Pelletization with spark plasma sintering and characterization of metal iodides: An assessment of long-term radioiodine immobilization options

Jared M. Oshiro,[(a)] Alessandra Lie Fujii Yamagata,[(a)] Saurabh Kumar Sharma,[(b)] R. Matthew Asmussen,[(a),*] Saehwa Chong,[(a)] Brian J. Riley,[(a),*] Jarrod V. Crum,[(a)] Joshua A. Silverstein,[(a)] Nathan L. Canfield,[(a)] and Jie Lian[(b),*]

[(a)]*Pacific Northwest National Laboratory, Richland, WA 99334*

[(b)]*Rensselaer Polytechnic Institute, Troy, NY 12180*

Keywords: iodine waste form, spark plasma sintering, metal-iodide compounds, semi-dynamic leach testing

Abstract

Four promising iodine "getter" materials (Ag, Cu, Bi, Sn) for radioiodine capture were assessed in their pure metal-iodide (MI_x) pelletized forms to compare relative chemical durabilities. To study chemical durability, commercial MI_x compounds of AgI, BiI_3, BiOI, CuI, and SnI_4 were converted to dense, monolithic pellets using spark plasma sintering. Semi-dynamic leach testing in the form of modified ASTM C1308 tests were then performed on the pellets in two different forms including unmounted (as-pressed) specimens (i.e., "U") and epoxy-mounted specimens (i.e., "M") with polished surfaces. The chemical durability results and sample characterizations showed that three of the five MI_x compounds tested (i.e., AgI, CuI, and BiOI) displayed moderate to high leach resistances. The remaining two MI_x compounds (i.e., BiI_3 and SnI_4), which are both desirable iodine waste forms due to their high iodine loading capacities, readily decomposed during leach testing indicated by crystallographic changes in the specimens as well as large amounts of iodine detected in the leachate solutions. The instabilities of BiI_3 and SnI_4 raise uncertainties for using the base metals/cations (i.e., Bi^0/Bi^{3+} and Sn^0/Sn^{4+}, respectively) as viable getters for radioiodine capture due to likely poor waste form chemical durabilities after capture and consolidation into waste forms.

[*] *Corresponding authors*: matthew.asmussen@pnnl.gov; brian.riley@pnnl.gov; lianj@rpi.edu

1 Introduction

Radioiodine capture and immobilization from nuclear processes and nuclear accidents are important environmental issues as it is highly mobile within the environment and, due to its incorporation into the thyroid gland, it poses a significant cancer risk even at low concentrations.[1-3] The most common iodine radioisotopes considered of interest include high-activity and short-lived ^{131}I ($t_{1/2}$ = 8.02 d) as well as low-activity and long-lived ^{129}I ($t_{1/2}$ = 1.57×10^7 y). Many studies have been conducted to evaluate methods and processes for capturing radioiodine released during nuclear processes such as vitrification and reprocessing, using liquid scrubbing (e.g., caustic scrubbers) and solid sorbents.[4-9] Solid sorbents often utilize a reactive getter metal or metal ion, such as Ag^0 or Ag^+, within a passive matrix (e.g., zeolite, aerogel) to form a metal-iodide compound, i.e., MI_x = AgI, in this case.

Once iodine is loaded into a sorbent, the material could either be stored onsite at the originating facility or subsequently converted into a waste form for disposal within a nuclear waste repository. While the initial effective capture portion of the process is extremely important, the long-term stability and chemical durability of the final form of the radioiodine (i.e., the compound containing the iodine) within a repository environment is of utmost importance. The chemical durabilities of Ag-based sorbents materials have been documented within the literature,[10-13] and the results show low release rates. However, Ag has disadvantages as it is a precious metal (it is expensive) and its disposal is controlled in the U.S. by the Environmental Protection Agency (EPA) under the Resource Conservation and Recovery Act (RCRA) through the Code of Federal Regulations 40 CFR Part 261.[14] Thus, several alternative materials with different getter elements (e.g., Bi-, Cu-, Sn-based sorbents) are gaining traction across the world as candidate replacement options to the Ag-based sorbents. While many of these new getter elements show promise when installed in a variety of passive supports (e.g., zeolites, aerogels, xerogels), the corrosion behaviors of these compounds within aqueous environments remain relatively unstudied, especially using standardized leaching procedures, e.g., from American Society for Testing and Materials International (ASTM).

The current study documents a set of experiments to evaluate the chemical durabilities of potential MI_x compounds that would form in proposed chemisorption-based solid sorbents as candidate hosts for long-term disposal of radioiodine based on previous studies, including AgI,[15-18] BiO_xI_y (i.e., BiI_3 and BiOI separately),[5,19-24] CuI,[16,18,25,26] and SnI_4.[16,18,27,28] Each of these getter elements has been considered as a potential sorbent for radioiodine disposal when embedded in a variety of (passive) matrices for the final waste form as metals and/or as ionic forms (e.g., Ag^0/Ag^+, Bi^0/Bi^{3+}, Cu^0/Cu^+, or Sn^0/Sn^{4+}).[11] Specifically for Bi-based sorbents, a wide range of compounds (e.g., BiOI, $Bi_4O_5I_2$, Bi_5O_7I, $Bi_7O_9I_3$) can be found within iodine-loaded sorbents;[5,29-31] however, only BiI_3 and BiOI were found to be commercially available for these experiments.

Since solid forms of these compounds were not commercially available, for these experiments, the pure MI_x compounds were produced in monolithic (pelletized) forms using spark plasma sintering (SPS) and tests were conducted using a modified ASTM C1308 procedure[32] based on previous experiments used for similar iodine waste forms.[10,33,34] The SPS process is a hot uniaxial pressing method utilizing pulsed or unpulsed current coupled directly to a graphite die whereby very rapid heating rates can be achieved (up to 1000 °C min^{-1}). SPS was selected for consolidation rather than other techniques such as hot isostatic pressing (HIP) on the basis of availability. The ASTM C1308 procedure is a semi-dynamic leaching test whereby sample coupons were subjected to a leachant and the leachant was replaced every 24 hours to maintain dilute conditions. More details are provided in Section 2 for these processes.

Until now, most waste form chemical durability studies focused primarily on the property assessment of MI_x compounds embedded in other matrices such as hot-pressed zeolite,[12,35] sodalite,[36] silica aerogel,[12] porous alumina,[37] aluminosilicate xerogel,[38] glass,[39,40] or cast stone.[41] Assessing pure MI_x compounds (without the passive matrix) was a research gap identified during a recent literature review[10] on the assessment of available standardized testing data for a variety of promising iodine waste form options. Before the SPS pelletization process, thermogravimetric analysis (TGA) and differential scanning calorimetry (DSC) were performed on the as-received chemicals. The SPS pellets were characterized using

X-ray diffraction (XRD), scanning electron microscopy (SEM), energy dispersive X-ray spectroscopy (EDS), as well as X-ray computed tomography (XCT) to evaluate the crystal structures, microstructures, phase distributions, elemental distributions, and porosities, respectively.

2 Experimental

2.1 Source Chemicals

The precursor chemicals for pellet fabrication used in this study were procured from Thermo Fisher Scientific in glass jars that contained a mixture of different particle sizes and were used without any additional treatments or purifications. Specific details for each of these chemicals are provided Table S1 (SI).

2.2 Thermogravimetric Analysis

TGA datasets were collected at Rensselaer Polytechnic Institute (RPI) with an SDT 650 instrument. Table S2 (SI) shows the heat-treatment profiles and isothermal holds were set based on the melting temperatures for the metal-iodide (MI_x) compounds[42] or regions in the TGA curves near which mass losses were observed. All heating rates (r_H) were 10 °C·min^{-1}. The data from these experiments were used to direct the starting heat treatment parameters for SPS experiments.

2.3 Spark Plasma Sintering

After TGA, SPS experiments were conducted at RPI under argon atmosphere within a 6-mm graphite die in a Model 10-3 SPS system (Thermal Tech. LLC, Santa Rosa, CA) under 50 MPa sintering pressures (P_s) and currents of 100 A – 200 A. The parameters used for each SPS pelletization experiment are provided in Table 1 and were selected using the mass-loss data determined using TGA analyses for guidance, including heating rates (r_H), cooling rates (r_C; N/A denotes no controlled cooling was used), sintering temperatures (T_s), and sintering times (t_s). Additional information provided in Table 1 includes material properties (where available) of bulk theoretical densities ($\rho_{b,t}$), melting temperatures (T_m), and solubility product constants (K_{sp}) for the pure MI_x compounds.[42,43] All pellets were prepared using small

masses of starting chemicals (m_p < 0.5 g; see Table S3, SI) targeting pellets with heights of ≈ 2 mm. In all cases, three separate pellets were made under like conditions while conditions between pellet sets differed substantially in some cases. The selection of a 120 °C T_s for AgI pellets was chosen to prevent extrusion of AgI from the die due to the β-AgI (hexagonal wurtzite) to α-AgI (body-centered cubic) structural transition at 147 °C based on trial runs at 150°C, 200 °C, and 400 °C before the final set of pellets was produced. Selections of T_s values for the other samples were made to minimize volatile losses during SPS processing.

Table 1. Parameters for SPS pellet production including heat rates (r_H), cooling rates (r_C; N/A denotes no controlled cooling was used), sintering temperatures (T_s), and sintering times (t_s) as well as material properties including bulk theoretical densities ($\rho_{b,t}$), melting temperatures (T_m), and solubility product constants (K_{sp}) are provided where possible for the pure MI_x compounds.[42-44] All pellets were produced using a 6-mm diameter graphite die under 50 MPa sintering pressures (P_s).

Sample	r_H (°C·min^{-1})	r_C (°C·min^{-1})	T_s (°C)	t_s (min)	$\rho_{b,t}$ (g·cm^{-3})	T_m (°C)	K_{sp}
AgI	25	25	120	2	5.675	558	8.52×10^{-17}
BiI_3	25	N/A	200	10	5.780	408.6	7.71×10^{-19}
BiOI	50	50	500	1	7.92	827	–
CuI	25	25	400	10	5.67	606	1.27×10^{-12}
SnI_4	100	100	100	1	4.56	143	–

Following SPS runs, pellets were removed from the graphite die and lightly polished with different SiC grinding papers to remove the graphite layer from interactions with the die. The samples were polished with 240 grit (coarse) and followed by 600 grit (fine). In some cases, residual graphite was observed for some pellets (e.g., see Figure S1, SI).

2.4 Chemical Durability Testing

Chemical durability tests were conducted on SPS pellets using the ASTM C1308 procedure[32] in ASTM Type I (deionized) water (DIW) with samplings at 24 h (1 day), 48 h (2 days), 72 h (3 days), 96 h (4 days), and 168 h (7 days) from test initiation to maintain consistency with previous testing performed on similar types of iodine waste forms.[10,33,34] Testing was performed without replicates on samples mounted in epoxy (called *mounted,* labeled with "-M" designations) to expose a single face of the pellet (Allied EpoxySet) and on unmounted monoliths with all sides exposed (called *unmounted,* labeled with "-U"

designations). The mounted samples were polished with up to 600 grit sandpaper, and the monoliths were unfinished. A "blank" epoxy puck without a sample was also run through the ASTM C1308 testing protocol to assess total organic carbon (TOC) and impurities released into the leachate. The mounted samples were prepared to save material and so that an accurate surface area measurement could be made on the exposed face of each sample.

The ratio of sample surface area to the solution volume ($SA \cdot V^{-1}$) was modified to 1 cm^2 to 20 mL ($SA \cdot V^{-1}$ = 5 m^{-1}), respectively, to allow for adequate specimen coverage within the leachant vessel. The tests were conducted at 90 °C in Savillex PFA jars with samples sitting on PFA perforated support grids, and with full leachant exchange at each interval. For the exchanges, the same vessels were used where the samples were removed, the leachate was removed (and saved), the sample was returned to the vessel, fresh leachant was added, the vessel was lidded, and returned to the oven. The concentrations of ^{127}I in solution were determined via inductively coupled plasma mass spectroscopy (ICP-MS), and the concentrations of the metallic cation (Ag, Bi, Cu, Sn) were determined by ICP optical emission spectroscopy (ICP-OES). Uncertainties with ICP-MS and ICP-OES values are ±10% of reported values. Detection limits in the form of estimated quantitation limit (EQL, $\mu g \cdot L^{-1}$) are reported in Table S9 (SI). The normalized losses (*NL*) of element "*i*" ($NL_{[i]}$, $g \cdot m^{-2}$) were determined with Equation (1),[45] where $c_{[i]}$ is the concentration of the element "*i*" in $g \cdot L^{-1}$, *V* is the volume of the solution added (L), *SA* is the surface area of the monolith (m^2), and f_i is the mass fraction of "*i*" in the unleached monolith ($g \cdot g^{-1}$). Cumulative normalized loss (*CNL*) of the element "*i*" through the *N*th interval ($CNL_{N[i]}$, $g \cdot g^{-1}$) was determined with Equation (2). The incremental fraction leached of ^{127}I ($IFL_{n[^{127}I]}$) was determined with Equation (3),[32] where $a_{n[^{127}I]}$ represents the mass (g) of ^{127}I measured during test interval "*n*", and $A_{0[^{127}I]}$ is the mass of ^{127}I in the specimen prior to leaching. Cumulative fraction of ^{127}I leached through the *N*th interval ($CFL_{N[^{127}I]}$, $g \cdot g^{-1}$) was determined with Equation (4).[32]

$$NL_{[i]} = \frac{c_{[i]} \cdot V}{SA \cdot f_i} \quad (1)$$

$$CNL_{N[i]} = \sum_{n=1}^{N} NL_{n[i]} \quad (2)$$

$$IFL_{n[^{127}\mathrm{I}]} = \frac{a_{n[^{127}\mathrm{I}]}}{A_{0[^{127}\mathrm{I}]}} \quad (3)$$

$$CFL_{N[^{127}\mathrm{I}]} = \sum_{n=1}^{N} IFL_{n[^{127}\mathrm{I}]} \quad (4)$$

2.5 Pellet Characterizations

Optical microscopy (OM) was performed on as-made pellets with a Keyence VHX-7000 system using different magnifications (i.e., 1×, 5×, 20×, 100×, and 500×) to assess appearances at these different conditions. Imaging was performed on both as-made SPS pellets and after chemical durability tests to assess the surface corrosion of the different pellets. The crystalline phase information of the SPS densified pellets were characterized using a Bruker® D8 Advance XRD system (Bruker AXS Inc., Madison, WI) with Cu K_α emission. The detector used was a LynxEye™ position-sensitive detector with a collection window of 3° 2θ. Scan parameters were 5–70° 2θ with a step of 0.015° 2θ and a 0.3-s dwell at each step. The SPS pelletized specimens were loaded into cavities of off-axis fused quartz holders (MTI Corporation; Richmond, CA). The SEM analyses were performed with a JSM-7001F field-emission gun microscope (JEOL USA, Inc.; Peabody, MA) and EDS was performed using a Bruker xFlash 6|60 (Bruker AXS Inc., Madison, WI).

The XCT measurements were performed on the post-leached "-U" specimens, as well as an unleached set of spare ("-S") specimens to investigate the uncertainties associated with the $SA \cdot V^{-1}$ calculations (samples of AgI-S broke during analysis and SnI_4-U was too brittle to measure). The measurements were made with a Zeiss Xradia Versa 610 X-ray microscope. Collection was done at 150 kV, 23 W, 8-s collection times per projection, and 2401 projections around a full 360°. An appropriate filter was utilized to maximize transmission through the material. A 0.4× objective lens set to 1×1 binning of the camera was selected in conjunction with the source and detector positioning to provide a 4-μm voxel size.

3 Results

3.1 Results of TGA on Raw Materials and SPS

The TGA data used for determining the optimal SPS temperatures for pelletization are shown in Figure 1. The data revealed some mass loss events attributed to a range of phenomena from minor mass losses attributed to adsorbed water (e.g., AgI) to full sample decomposition (e.g., BiOI). The mass losses were notably different based on the T_m values, thermal stabilities (and decompositions), and crystallographic changes for each MI_x compound. The SPS processing temperatures used were selected specifically to keep the consolidation process below the temperature at which decomposition was expected and produce high-density pellets representative of the starting materials. The temperature at which BiOI appears to lose the most mass is at $T > 600$ °C, but the reported decomposition temperature for this compound is ≈ 300 °C (see Table S11, SI)[42] and the T_m is reported to be as high as 827 °C (see Table 1);[44] the difference in measured and reported values is unclear.

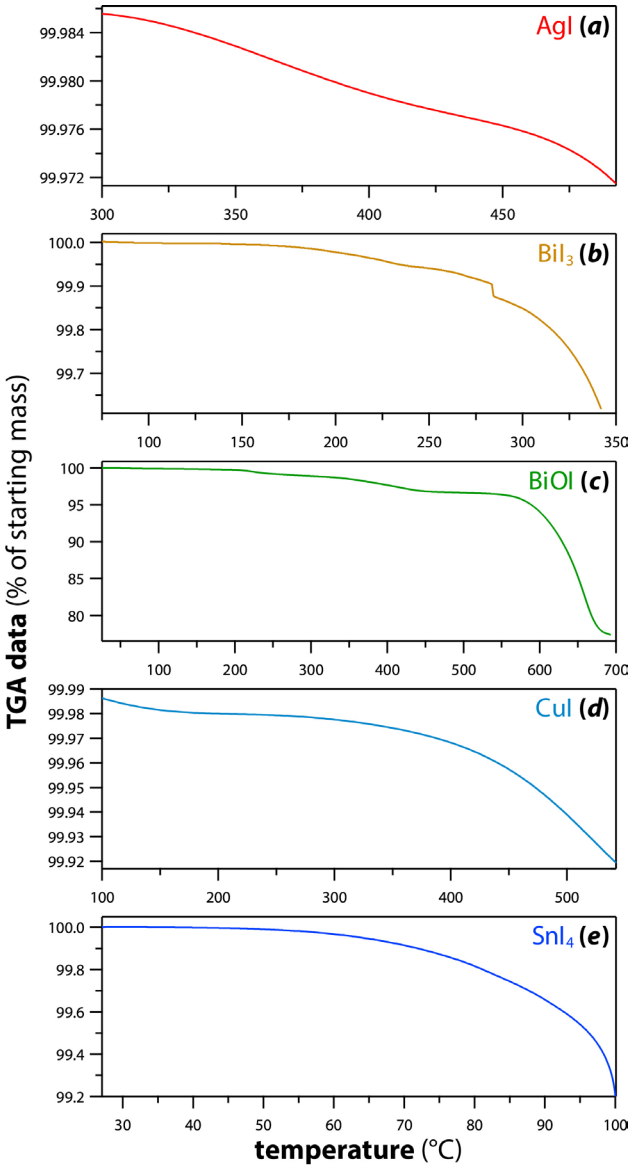

Figure 1. TGA data for starting materials, including (a) AgI, (b) BiI_3, (c) BiOI, (d) CuI, and (e) SnI_4. This data was used to direct the sintering temperature (T_s) selection for SPS pelletization experiments.

The measured pellet densities following SPS processing are documented in Table S3 (SI) along with examples of sample masses (m_p) used to produce SPS pellets for the different samples. It is clear from this table that the measured pellet densities (ρ_{meas}) differed in some cases from the expected (theoretical) pellet bulk densities based on literature values ($\rho_{b,t}$). Note that the differences between ρ_{meas} and $\rho_{b,t}$ values is, at least in part, due to the formation of other crystalline phases in the samples during the SPS processing (e.g., SnI_2 formation for the SnI_4 pellet), but also attributed to residual porosities in the fired pellets.

3.2 Chemical Durability Testing Results

The $CNL_{N[^{127}\mathrm{I}]}$ values for all pellet specimens over the full 7-day test periods are summarized in Table 2 and are illustrated in Figure 2. The $NL_{[i]}$ values provided in Table S7 (SI) show that, in some cases, the "-M" samples showed higher initial releases (day-1) than "-U" samples (i.e., AgI, BiOI, SnI_4) whereas for others (i.e., CuI, BiI_3), the opposite was true. The $CFL_{N[^{127}\mathrm{I}]}$ values of ^{127}I can be retrieved from Table S6 (SI) and these are also shown in Figure 3 for the "U" specimens. The TOC of the epoxy blank was 73.7 $\mu g \cdot L^{-1}$, and other ions analyzed by ICP-OES were below detection limits. The *SA* values used to calculate $CNL_{N[i]}$ as determined geometrically or by XCT can be found in Table S10; the XCT images are shown in Figure S15 and Figure S16 (SI).

Table 2. Cumulative normalized loss ($g \cdot m^{-2}$) of ^{127}I ($CNL_{N[^{127}\mathrm{I}]}$) in the SPS specimens following the modified ASTM C1308 procedure. Uncertainties related to $c_{[i]}$ values are ±10% and additional uncertainties are present from the *SA* calculations [see Equation (1) and Equation (2)]. Here, RSQ values denote the Pearson Correlation Coefficient for days 1-4. Slopes and intercepts were calculated from data fits for days 1-4 and the slopes correlate to the normalized dissolution rate (*NDR*) ($g \cdot m^{-2} \cdot d^{-1}$).

Sample ID	$CNL_{N[^{127}\mathrm{I}]}$ values ($g \cdot m^{-2}$; *N* in days)					Data fitting (days 1–4)		
	N = 1	*N* = 2	*N*= 3	*N* = 4	*N* = 7	RSQ	*NDR* ($g \cdot m^{-2} \cdot d^{-1}$)	Intercept
AgI-M	2.13E-02	2.34E-02	2.46E-02	2.51E-02	3.00E-02	0.93	1.28E-03	2.04E-02
AgI-U	1.08E-02	1.25E-02	1.42E-02	1.55E-02	1.75E-02	1.00	1.59E-03	9.26E-03
BiI_3-M	8.77	10.53	11.7	12.24	12.89	0.95	1.16E+00	7.91E+00
BiI_3-U	36.55	45.57	51.73	54.02	67.56	0.94	5.86E+00	3.23E+01
BiOI-M	12.03	12.32	12.46	12.53	12.66	0.92	1.64E-01	1.19E+01
BiOI-U	3.67	3.85	3.97	4.08	4.29	0.98	1.36E-01	3.55E+00
CuI-M	0.22	0.72	1.15	1.58	2.14	1.00	4.50E-01	-2.10E-01
CuI-U	0.93	1.98	2.49	2.89	3.68	0.95	6.38E-01	4.77E-01
SnI_4-M	251.71	264.64	267.82	268.92	269.89	0.80	5.48E+00	2.50E+02
SnI_4-U	126.35	132.76	133.57	134.08	135.42	0.74	2.40E+00	1.26E+02

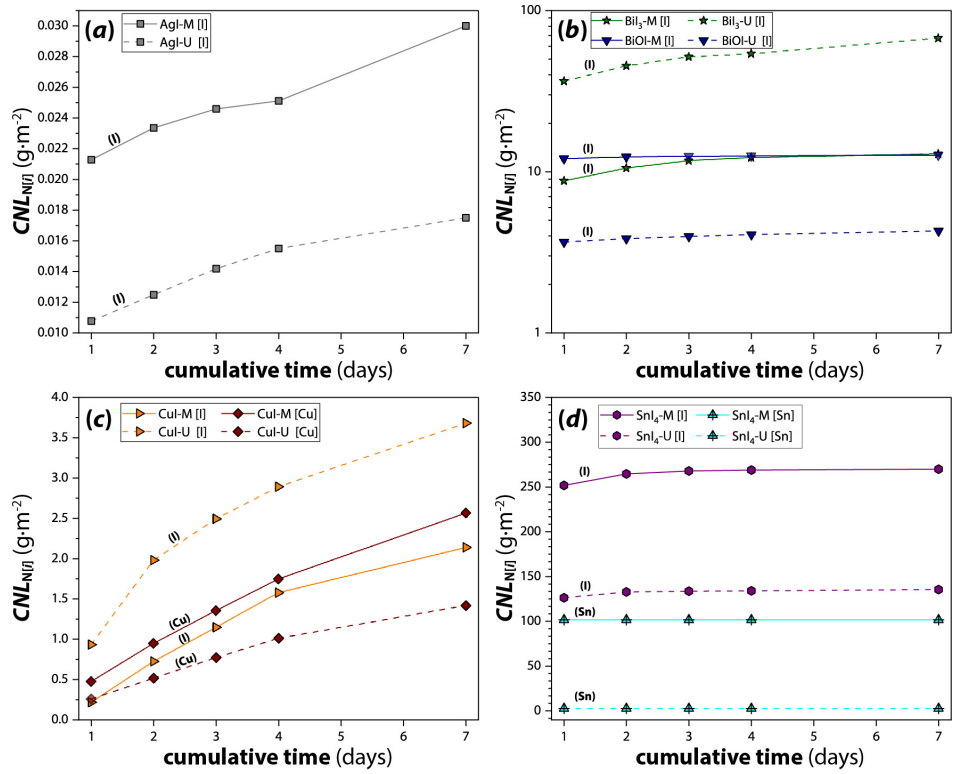

Figure 2. $CNL_{N[i]}$ values for the SPS specimens following the modified ASTM C1308 procedure including (a) AgI, (b) BiI_3 and BiOI, (c) CuI, and (d) SnI_4. Note that (b) is reported in log_{10} scale.

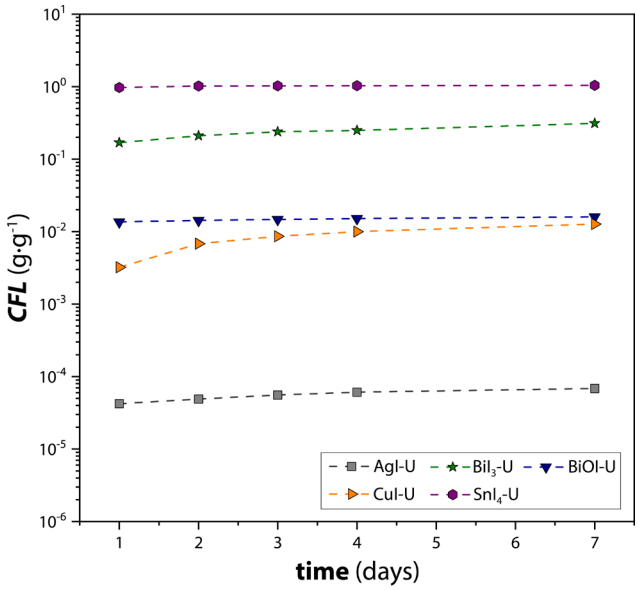

Figure 3. $CFL_{N[^{127}I]}$ values for "U" specimens following the modified ASTM C1308 procedure.

3.3 OM Results

The OM images of the as-fabricated unmounted and mounted pellets are provided in Figure 4a and Figure 4c, respectively. Some inter-pellet heterogeneities are present for most pellets and intra-pellet heterogeneities are observed between replicates in each set of pellets in terms of appearance; this includes different colors and gradients as well as pits and voids being observed in some samples and not others. The appearances of pellets were as follows: AgI pellets were light gray to tan, BiI_3 pellets were dark gray to black, BiOI pellets were purple to dark pink, CuI pellets were black, and SnI_4 pellets were bright yellowish orange. Additional imaging of all produced pellets (in triplicate) are provided in the SI for AgI (Figure S1), BiI_3 (Figure S2), BiOI (Figure S3), CuI (Figure S4), and SnI_4 (Figure S5). OM images of the unmounted and mounted specimens after leach testing are provided in Figure 4b and Figure 4d, respectively, where clear visual differences are apparent between the four series of pellets. Note that in the case of BiI_3-U, the color transition only occurred partially as a layer, as evidenced in the cross-sectioned pellet (see Section 4). In addition, distinct phase segregations were observed in the CuI-U and SnI_4-U specimens. These specific areas and their phase boundaries were analyzed in more detail with SEM and EDS analysis (Section 3.5 and discussion in Section 4).

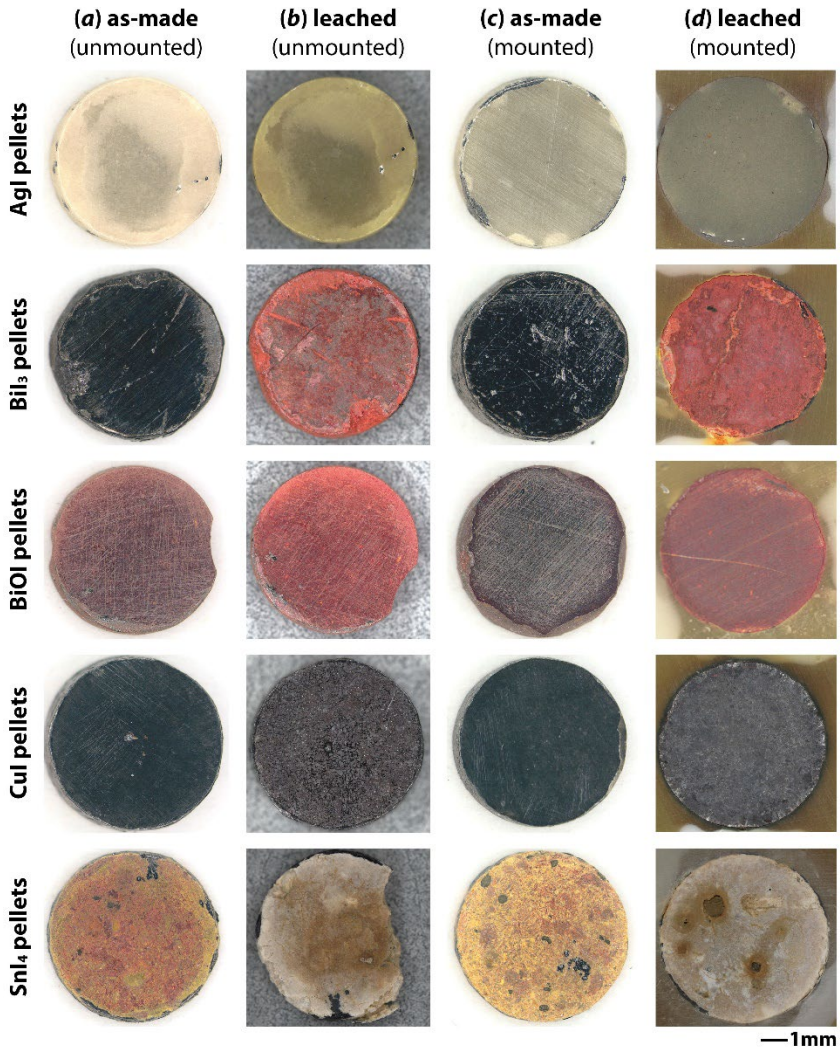

Figure 4. Optical micrographs of the SPS pellets (a) as-made unmounted samples, (b) unmounted samples after leach testing, (c) as-made mounted samples, and (d) mounted samples after leach testing.

3.4 XRD Results

The XRD data for all pellets following the SPS process are summarized in Table S5, with specific data provided in the SI, including Figure S10 (AgI), Figure S11 (BiI_3), Figure S12 (BiOI), Figure S13 (CuI), and Figure S14 (SnI_4). The primary phases for all samples aligned with the target phases with the exception of the SnI_4 pellets showing evidence of SnI_2 formation [i.e., loss of I_2 during SPS – see Equation (5)] and some pellets with residual graphite from SPS. The conversion of SnI_4 to SnI_2 is corroborated by the

increased pellet densities (see Table S3, SI) for these specimens since the density of SnI_2 is higher than that of SnI_4 (see Table S12, SI).

$$SnI_4 \xrightarrow{\Delta} SnI_2 + I_{2(g)} \quad (5)$$

Figure 5 shows the XRD patterns of the "M" pellets before and after the ASTM C1308 chemical durability test. The post-leach results indicate that the AgI, BiOI, and CuI specimens remained relatively stable during the testing period. The AgI pellet retained both β-AgI (*P*6$_3$*mc*) and γ-AgI (*F*-43*m*) phases throughout the testing period, with the data showing an increase in relative peak intensity of hexagonal β-AgI. Likewise, the BiOI and CuI pellets maintained their crystal structures post testing, with a few exceptions. In the BiOI specimen, a minor phase was observed at ~29° 2θ before modified ASTM C1308 tests (see Table S5, SI) and attributed to bismuth oxide ($Bi_2O_{2.33}$). However, it was difficult to confirm the specific phase present based on a single peak, and this phase was also stable during the chemical durability test. For the CuI pellet, the formation of Cu_2O was observed at ~36° 2θ after the test (further evidence of the Cu_2O phase is discussed in Section 4).

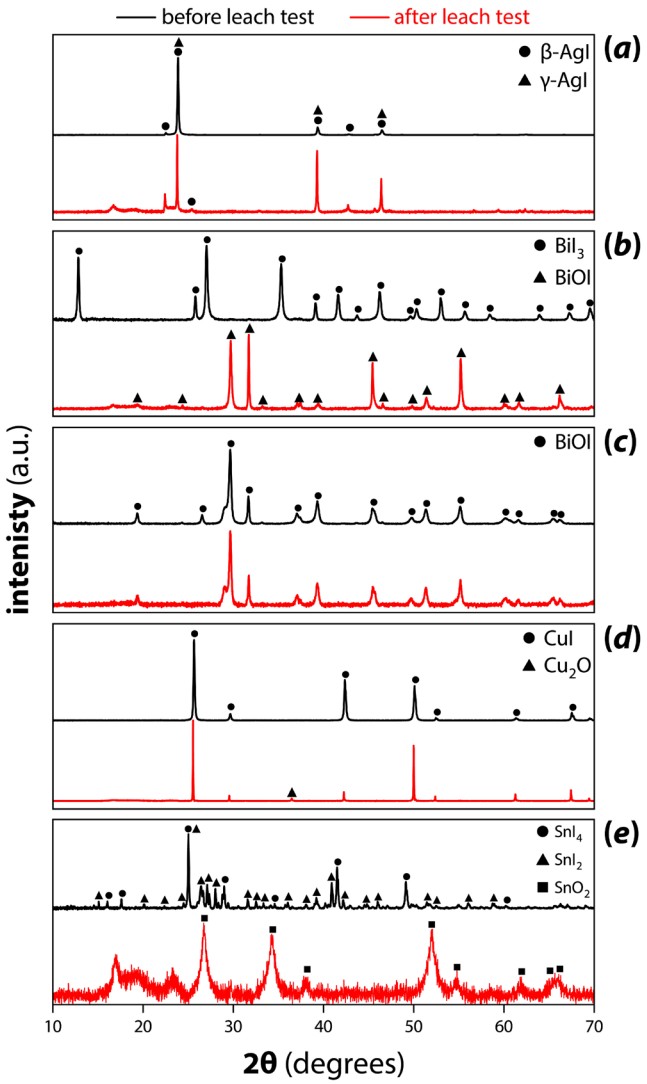

Figure 5. XRD patterns of "M" pellets including (a) AgI-M, (b) BiI_3-M, (c) BiOI-M, (d) CuI-M, and (e) SnI_4-M before and after modified ASTM C1308 chemical durability testing.

The XRD results on the leached pellets illustrate the instability of the BiI_3 and SnI_4 specimens. For the BiI_3 pellet, BiI_3 was converted to BiOI during leaching, but only on the surfaces of the pellet where the core remained as BiI_3, indicating a reaction had occurred, which resulted in the formation of a more stable compound during chemical durability testing (see Section 4 for more information). For the SnI_4 pellet, two different iodides of Sn (i.e., SnI_4 and SnI_2) were present after SPS. These two phases decomposed during the chemical durability test, and formation of SnO_2 was observed. The wider peaks of SnO_2 compared to SnI_4 and SnI_2 suggested smaller crystallite size of SnO_2; the diffraction peak intensities were also very low

in the leached sample compared to the pre-leached analysis suggesting some amorphization occurred during the chemical durability testing.

3.5 SEM-EDS Results

Quantitative EDS analysis was performed on each of the "M" specimens after leach testing, with additional analysis performed on the unmounted pellets that exhibited phase separations and crystallization of secondary phases, e.g., see Figure 6 for CuI-U, Figure S6 (SI) for CuI-U, and Figure S7 (SI) for SnI_4-U. The EDS data was compiled from average analyses of 16 separate regions throughout the bulk material of the "M" specimens and a summary of the elemental distributions is provided in Table 3, which has been renormalized to exclude carbon from the residual graphite left on the surface. The ~3 at.% phosphorus in the SnI_4 sample is attributed to contamination within the source chemical.

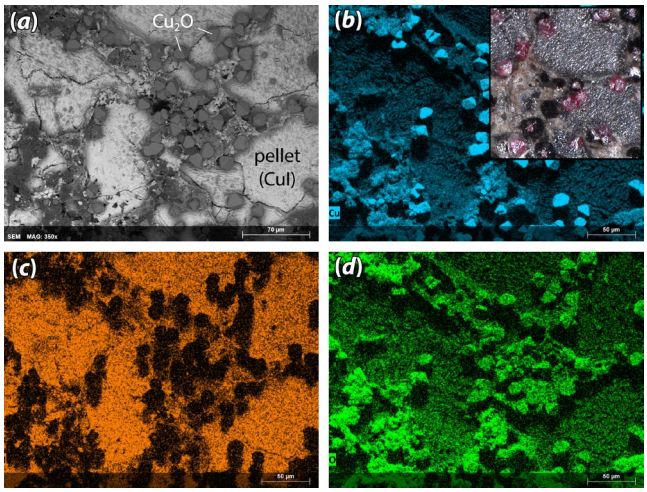

Figure 6. SEM and EDS imaging of the crystallization observed in the CuI-U specimen, including (a) a backscattered electron SEM micrograph at 350× and (b-d) EDS maps of (b) Cu, (c) I, and (d) O. The Cu-O phase was determined to be Cu_2O based on appearance and EDS analysis. The inset in (b) is an OM micrograph taken in a different location and shows the appearance of the Cu_2O crystals.

Table 3. EDS elemental distributions of the mounted specimens after chemical durability testing reported in atomic % (at.%) with standard deviations (±1σ) shown below the values in parenthesis. Values had been renormalized to remove carbon (graphite). "ND" denotes non-detect.

Sample	I	O	Ag	Bi	Cu	Sn	P
AgI-M	49.8 (±1.1)	2.0 (±1.0)	48.2 (±0.8)	ND	ND	ND	ND
BiI_3-M	36.1	23.3	ND	40.5	ND	ND	ND

	(±2.1)	(±2.8)		(±0.9)			
BiOI-M	28.3 (±2.3)	29.1 (±2.3)	ND	42.7 (±0.7)	ND	ND	ND
CuI-M	59.0 (±0.6)	ND	ND	ND	41.0 (±0.6)	ND	ND
SnI_4-M	0.3 (±0.3)	63.6 (±1.3)	ND	ND	ND	33.4 (±1.2)	2.7 (±0.4)

4 Discussion

The AgI pellets displayed the least amount of cumulative leaching compared to the other specimens, with values being one or more orders of magnitude lower than the other specimens when comparing *CNL* (Figure 2) and *CFL* (Figure 3). This is expected due to the low solubility of AgI in water.[10,11,42] Silver concentrations for both AgI specimens were below the detection limits of the ICP-OES equipment (1400 $\mu g \cdot L^{-1}$), highlighting the prior success shown for Ag-based sorbents converted to waste forms.[10]

The SnI_4 specimens exhibited the highest quantity of iodine leaching, which is attributed to the conversion to SnO_2 as evidenced by the high concentrations of iodine (see Figure 2d) in the leachates, as well as the color of the leachate solution being yellow. The $CNL_{N[Sn]}$ values are notably lower than those of $CNL_{N[I]}$ for both the SnI_4-M and SnI_4-U specimens, but the $CNL_{N[Sn]}$ values are still rather high for SnI_4-M. These data together with the XRD data (see Figure 5) reveal that the SnI_4 coupons degraded through a combination of both SnI_2/SnI_4 dissolution and the formation of SnO_2. The presence of SnO_2 after corrosion could be due to the loss of iodine in different ways by the reactions shown in Equation (6), Equation (7), and Equation (8).[46] The formation of SnO_2 is likely related to the hydrolysis of SnI_4 to form $Sn(OH)_4$, an intermediate resulting in SnO_2. Upon exposure to air, the solution can react to release I_2 into solution [see Equation (8)]. Likewise, the formation of SnO_2 and HI by hydrolysis of SnI_4 is shown in Equation (6) and Equation (9),[47] and further reaction of HI with O_2 can lead to I_2 formation [Equation (8)]. Another possible reaction for SnO_2 formation from SnI_2 is shown in Equation (7) where decomposed I_2 from SnI_4 can react with SnI_2 and water to form HI and SnO_2.

$$SnI_4 + 2\,H_2O \rightarrow SnO_2 + 4\,HI \quad (6)$$

$$I_2 + 2\,H_2O + SnI_2 \rightarrow 4\,HI + SnO_2 \quad (7)$$

$$4\,HI + O_2 \rightarrow 2\,I_2 + 2\,H_2O \quad (8)$$

$$SnI_4 + 4\,H_2O \rightarrow Sn(OH)_4 + 4\,HI \quad (9)$$

Similarly, the BiI_3-U specimen also exhibited a high release of iodine into solution, possibly by means of Equation (10) or by hydrolysis shown in Equation (11). Also, the $NL_{[Bi]}$ (and thus $CNL_{N[Bi]}$) values were below the detection limit of the instrument for all four specimens. Further characterizations summarized in Figure 7, Figure S9 (SI), and Table S4 (SI) indicated that this was a partial conversion of the BiI_3 core into a BiOI shell layer that formed around the exposed area of the pellet. It is unclear how passivating this BiOI shell layer was in terms of slowing release of the elements from the BiI_3 core, but the $CNL_{N[Bi]}$ data in Figure 2b for all Bi-based coupons do show reduction of the release rates over time, especially after initial high releases on day-1. The XRD results on the corroded pellets confirmed the presence of BiOI (see Figure 5). Higher I release occurred in the unmounted specimen (BiI_3-U), with the mounted BiI_3-M sample leaching a more moderate amount of I, like the BiOI-M sample. This difference in $CNL_{N[I]}$ values between the BiI_3-U and BiI_3-M pellets is attributed (at least partially) to the difference in available (internal) *SA* between the mounted and unmounted specimens where the use of epoxy in the latter samples reduced the leachant accessibility into the interior of the pellets. The $CNL_{N[I]}$ values for the BiOI-U and BiOI-M pellets show the opposite trend but still have very similar leaching behaviors. A similar type of analysis as shown in Figure 7 was planned for the SnI_4-U pellet, but due to its brittleness, it fractured completely after removing it from the SEM mount used for the SEM-EDS analysis.

$$2\,BiI_3 + O_2 \rightarrow 2\,BiOI + 2\,I_2 \quad (10)$$

$$BiI_3 + H_2O \rightleftarrows BiOI + 2\,HI \quad (11)$$

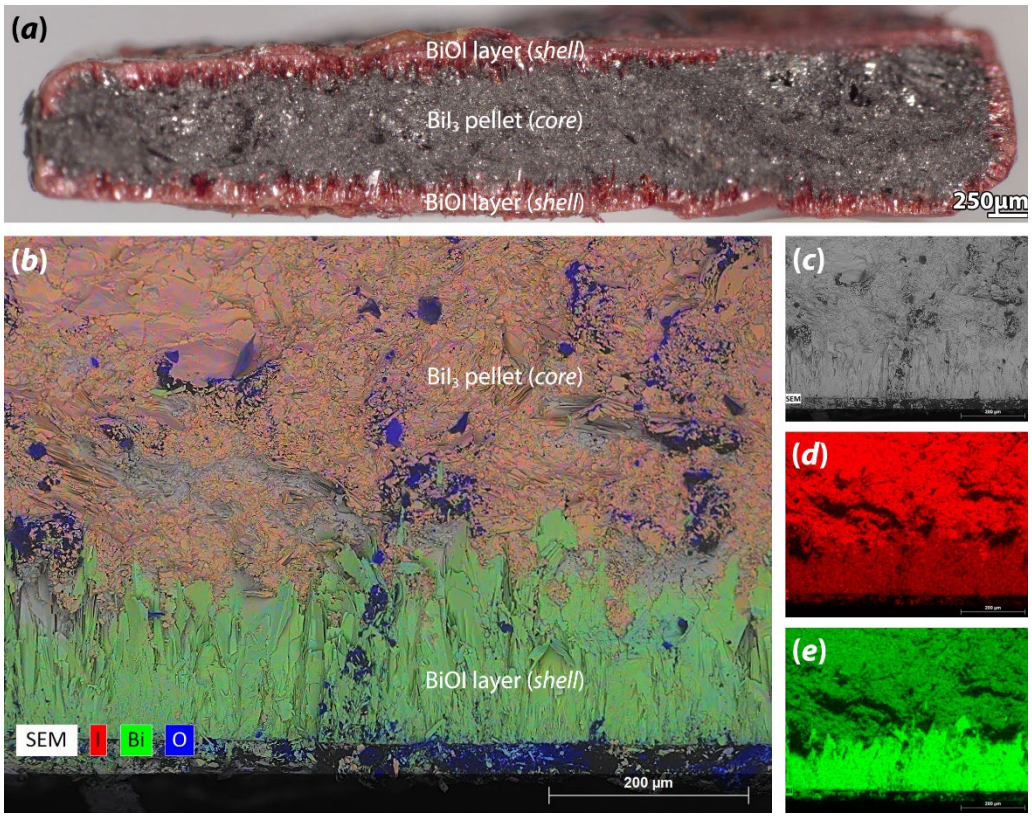

Figure 7. Cross-sectional view of the BiI_3-U pellet after leaching including (a) OM, (b) the EDS phase dot map (on the edge of the sample at the interface), (c) the SEM micrograph, (d) the EDS map of I, and (e) the EDS map of Bi. The labels shown in parts (a) and (b) show the BiI_3 core of the original pellet and the BiOI shell that is growing from the outside of the pellet inwards towards the core.

Similar behavior to the features seen in Figure 7 were observed in a previous study by Yang et al.[48] where dissolution of $Cs_3Bi_2I_9$ resulted in the formation of the secondary crystalline BiOI phases. In the Yang et al.[48] study, the BiOI layer formation was attributed to the dissolution-reprecipitation process; this is comparable to the data shown for the BiI_3-U pellet in Figure 7b. The kinetics of BiOI formation are rapid and once formed, it can greatly slow down the elemental release of iodine.

The CuI samples had the second lowest level of iodine released with respect to the other specimens, and also leached low quantities of Cu, which is attributed to the low solubility of CuI in water (see K_{sp} in Table 1 and water solubility data in Table S11, SI).[42] In addition, the higher release of iodine observed in the CuI-U compared to the CuI-M sample are likely due to the differences in *SA* values. Figure S8 (SI) shows Cu_2O crystals present on the surface of CuI-U (Figure 6),[49] potentially due to reprecipitation of Cu

from solution. However, their sparse distribution is unlikely to account for the higher release of iodine compared to the CuI-M sample, which is most likely due to the lower *SA* of the latter. A lower amount of copper was detected in the leachate of the CuI-U sample compared to CuI-M, which may reinforce this theory of reprecipitation. It is important to note that other studies that performed corrosion testing under different conditions found that reducing conditions have the potential to increase the leach rates of CuI.[25]

In Figure 8, the ^{127}I concentrations ($mg \cdot L^{-1}$) are compared to theoretical solubilities based on K_{sp} values at room temperature (22–25 °C). While the concentration of the ions exceeded what was expected based on the K_{sp} data, the K_{sp} values assume standard conditions (which was not the case for the current study) and only simple aqueous dissolution is taking place. However, the test was performed at 90 °C, and several other factors (particularly kinetics and thermodynamics) can influence this, including the release of I_2 due to partial or full decompositions of BiI_3 [see Equation (8), Equation (10), and Equation (11)] and SnI_4 [see Equation (6), Equation (7), and Equation (8)]. The release rates are also affected by the *SA* values of the pellets and the presence of passivation layers and/or secondary phase formation on the pellet surfaces after initial reactions with the leachant.

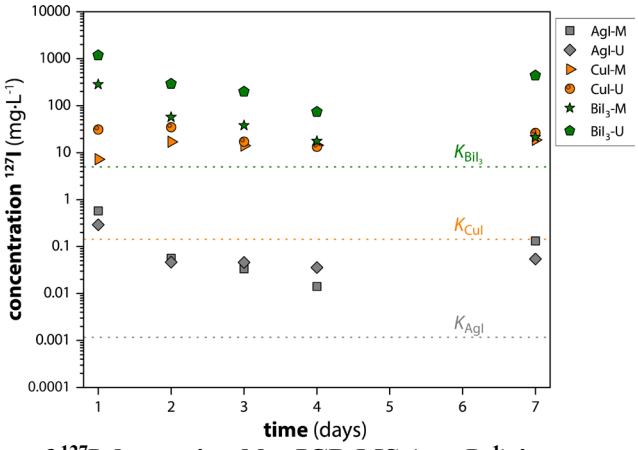

Figure 8. Concentration of ^{127}I determined by ICP-MS ($mg \cdot L^{-1}$) in comparison to the maximum solubility of ^{127}I based on K_{sp} at 25 °C for available pure compounds.[42] Time (days) is non-cumulative and where "$K_{[x]}$" represents the max solubility of iodine based on the K_{sp} of the compound "x".

The AgI SPS specimens in this work were compared to similar SPS-processed AgI-containing waste forms in the form of iodine-loaded Ag-functionalized silica aerogels in a previous study (Figure 9)[34]

where the aerogel samples are referred to as Aero-4, Aero-6, and Aero-7; LTE-2 refers to Ag-functionalized silica aerogel vitrified within a low-melting glass.[34] The SPS specimens created for the previous study released lower quantities of iodine (≈ 2–3 orders of magnitude) leached over the same time interval (4 days) with the same testing protocol (i.e., ASTM C1308) used in the current study. The specimens from the previous study[34] were dense and consolidated monoliths where only the outer surfaces were available for leaching, i.e., the geometric *SA*. The current results can be compared with the aerogel samples from the previous study,[34] which likely contained more residual porosity (and higher *SA* values), since the starting material was an aerogel, resulting in higher $CNL_{N[I]}$ values. In addition, the aerogel specimens were subject to some degree of matrix dissolution and were noted to have both individual AgI particles and clusters of AgI particles dispersed throughout the samples, as indicated by the voids left in the surface of the matrix.[34] The dissolution of the matrix material allows for the transport of the water (leachant) into the core of the sample and the dissolved species out of the matrix material to occur more easily; this leaching behavior is also accelerated by the higher *SA* within the core of the aerogels. The normalized dissolution rate (*NDR*) values of the pellets (Table 2) are compared against literature values reported in Reiser et al.[10] for other iodine waste forms in Table S8 (SI). Here, the *NDR* values of the pellets vary from sample to sample; however, the bulk material pellets analyzed in this study are, at the very least, on the same order of magnitude as other iodine waste forms documented within the literature.

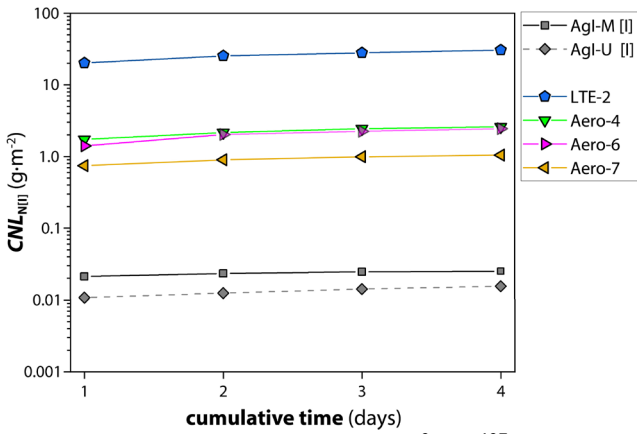

Figure 9. Comparison of cumulative normalized loss ($g \cdot m^{-2}$) of ^{127}I in AgI waste forms. Here, AgI-M and AgI-U refer to the SPS IWFs detailed in this paper, LTE-2 refers to Ag-functionalized silica aerogel vitrified within a low-melting glass[34] whereas Aero-4, Aero-6, and Aero-7 refer to SPS-consolidated Ag-functionated silica aerogel specimens at various iodine loadings.[34]

The color change in the SnI_4 samples from red-orange to a milky off-white (post leach test) reinforces that the SnI_4 converted to SnO_2 during leach testing (Figure 5e for SnI_4-M). Similarly, the BiI_3 specimen changed from a dark gray to black to red post leach test. Red is a typical color associated with BiOI,[50,51] which is another indication of decomposition as discussed previously. Microscopic dark red Cu_2O crystals formed on the surface of the CuI-U pellet (see Figure S8, SI).

As discussed previously, the BiI_3 and SnI_4 specimens underwent significant corrosion. The conversion of BiI_3 to BiOI by irradiation or simple heat-treatment around 280–300 °C has been documented in the literature,[52,53] and has been observed to occur even at room temperature [Equation (10)].[43] However, the XRD data summarized in Figure 5b suggests that BiI_3 was the dominant phase upon SPS processing because of a well-controlled environment with low oxygen content. After durability testing, the surface layers of the BiI_3-U (Figure 7) and BiI_3-M (Figure 5b) pellets were transformed to BiOI as evidenced by XRD and SEM-EDS, implying that the conversion of the BiI_3 to BiOI likely occurred only during leaching. Because of this, an additional possible reaction pathway for this decomposition could be the hydrolysis of BiI_3 shown in Equation (11).[43,50]

The elemental distributions of the "M" specimens after leach testing are provided in Table 3 and provide several key points. Firstly, the AgI specimen exhibits an approximate 1:1 molar ratio between

iodine and silver (as expected based on stoichiometry), which suggests that significant degradation did not occur. Conversely, the results show that SnI_4 had extremely low amounts of iodine remaining in the sample (≈ 1 at%), instead containing a large percentage of oxygen (≈ 61 at%). This agrees with the conversion of SnI_4 to SnO_2 discussed above. Lastly, the elemental makeups between both Bi-based pellet sets (i.e., BiI_3 and BiOI) were similar. The high oxygen content of the BiI_3 specimen and its similar iodine content to BiOI is documented in Figure 7, Table S4 (SI), and Figure S9 (SI). Further analysis of the cross-sectioned BiI_3-U pellet indicated that the average thickness of the BiOI layer was 188 (±27) μm (Figure 7).

Comparisons of the *SA* calculated geometrically for the "U" pellets (after leaching) and by XCT for the "U" and "S" pellets suggests that the volume of leachant used in the chemical durability testing was likely higher than needed to meet the target $SA \cdot V^{-1}$ (i.e., too high of $SA \cdot V^{-1}$ ratios were used based on XCT values alone) and the actual *SA* values were between these two measurements based on residual pellet porosities following SPS. The XCT *SA* calculation has some associated errors including voxel size limitations (limited resolution) and the *SA* calculations provide the full *SA* present in the sample, even if a portion is inaccessible (i.e., closed porosity) to the leachant. This, however, is contrary to most of the *CNL* results (Figure 2), which depicts the iodine release of the unmounted samples for some of the metal iodides as being lower than the mounted counterparts. Large initial releases followed by subsequent slower releases over the intervals is attributed to the initial dissolution of the exposed outer surface of each pellet. However, as leach time progresses a depleted or passive layer could form on the surface slowing release, as evidence by the optical microscopy images. Blank samples did not show any contamination from the system components or leachants, and all elemental releases are attributed to the samples themselves. A multitude of factors could contribute to this, which may include but not limited to the presence of residual graphite from the SPS process serving as a protective barrier layer, which was particularly present around edge face of the sample, varied surface finishes, and the removal of surface layers during polishing.

Lastly, it is also worth considering the possible formation of Cl and/or Br versions of these same metal-iodide and metal-oxyiodide compounds, i.e., AgX, BiX_3, BiOX, CuX, and SnX_4 (X = Cl, Br), since

nuclear waste streams can contain mixtures of these different halides.[7,54-56] Based on data acquired for the summary provided in Table S11 (SI), it appears that the documented water solubilities for the same compounds in each series are within a few orders of magnitude of each other while the K_{sp} values can range several orders of magnitude with the iodides showing lower values in cases where values were found for a given set of compounds (i.e., AgX, CuX). Since the properties of different halide versions of the same compounds will always vary, this needs to be taken into consideration when designing sorbents that can capture a range of halide gases present within a given stream if some of the metal-based or ion-based getters will produce compounds with unfavorable properties.

5 Summary and Conclusions

In total, five different iodine waste forms (i.e., AgI, BiI_3, BiOI, CuI, and SnI_4) were prepared as 6-mm diameter pellets in triplicate from pure host phases via SPS at various heating rates ranging from 25–100 °C·min^{-1}, hold times from 1–10 min, and sintering temperatures from 100–500 °C (see Table 1). These specimens were subject to semi-dynamic leach testing via a modified ASTM C1308 test protocol in DIW to analyze chemical durabilities. These tests were carried out on polished epoxy-mounted samples ("-M") with nearly identical surface areas as well as unmounted pellets ("-U") without surface finish; note that the third pellet from each set ("-S") were reserved as spares. Performance differences between mounted and unmounted samples varied for all sample sets. The XRD results showed that the structures of AgI, BiOI, and CuI pellets were stable during the chemical durability tests, which was consistent with the $CNL_{N[I]}$ values that indicated less iodine was release from each of these pellets compared to BiI_3 and SnI_4 pellets. Both XRD and SEM/EDS were used to confirm the degradation of the BiI_3 (into BiOI) and SnI_4 (into SnO_2) specimens.

The AgI pellets exhibited the best aqueous durability in comparison to the other specimens, which is due to its low solubility in water (Figure 8). The CuI pellets exhibited good leach resistance with respect to the other samples, also due to its low K_{sp} (see Table 1),[42] where it gradually released small amounts of both iodine and copper into solution over the testing duration. However, some minor Cu_2O crystallization

was observed on one face of the unmounted sample. The CuI-M sample also has evidence of reduced Cu release, that would support the idea of reprecipitation of the Cu if it were saturated in the bulk solution.

Two Bi-based specimens were tested in the forms of BiI_3 and BiOI, with larger quantities of iodine being leached from BiI_3 than BiOI, despite its lower K_{sp} (see Table 1).[42] This is likely due to the observed partial decomposition of BiI_3, leading to the release of additional I_2 into solution. Analysis of the XRD data before and after corrosion testing suggests that this decomposition occurred during the corrosion test process.

Of the five materials tested, SnI_4 had the worst chemical durability by far, with high quantities of iodine leaching within the first test interval of 24 hours. Similarly to the BiI_3 sample, the high release of iodine was likely due to the decomposition of SnI_4. In addition, XRD results showed the presence of SnI_2 prior to corrosion testing indicating that the SnI_4 was at least partially reduced during the SPS process or was an impurity in the as-received material.

Despite their potential for high iodine loading, the poor stability and corrosion performance of the BiI_3 and SnI_4 suggests that these compounds are less viable waste form candidates for long-term radioiodine disposal. However, other testing conditions, such as reducing environments and the presence of other ions, can play a significant factor in the performance and viability of these iodine waste forms, such as the case in AgI[12] and CuI.[25] The compound of BiOI has potential as an iodine waste form, but it has the lowest iodine loading (on a mass basis) of all the compounds tested. The limitation of using non-precious metals for gettering iodine is their inherent affinity for oxide conversion over iodide conversion based on thermodynamic data. These types of issues need to be considered in a holistic approach (i.e., cradle to grave) when designing next-generation iodine sorbents with the resulting iodine waste forms.[57]

6 Associated Content

Supporting Information

The Supporting Information is available free of charge at https://pubs.acs.org/.

TGA parameters; post-SPS measurements on pellets; additional OM, SEM, and EDS data; additional XRD data; supplementary chemical durability data; additional XCT data; physical properties of other metal-halide compounds (i.e., Cl, Br) that could form along with metal-iodide compounds.

7 Author Information

Corresponding Authors

R. Matthew Asmussen – Pacific Northwest National Laboratory, Richland, WA 99334, United States; email: matthew.asmussen@pnnl.gov

Brian J. Riley – Pacific Northwest National Laboratory, Richland, WA 99334, United States; email: brian.riley@pnnl.gov

Jie Lian – Rensselaer Polytechnic Institute, Troy, NY 12180; email: lianj@rpi.edu

Authors

Jared M. Oshiro – Pacific Northwest National Laboratory, Richland, WA 99334, United States

Alessandra Lie Fujii Yamagata – Pacific Northwest National Laboratory, Richland, WA 99334, United States

Saurabh Sharma – Rensselaer Polytechnic Institute, Troy, NY 12180

Saehwa Chong – Pacific Northwest National Laboratory, Richland, WA 99334, United States

Jarrod V. Crum – Pacific Northwest National Laboratory, Richland, WA 99334, United States

Joshua A. Silverstein – Pacific Northwest National Laboratory, Richland, WA 99334, United States

Nathan Canfield – Pacific Northwest National Laboratory, Richland, WA 99334, United States

8 Acknowledgements

Pacific Northwest National Laboratory (PNNL) is operated by Battelle Memorial Institute for the DOE under contract DE-AC05-76RL01830. This work was funded by the U.S. Department of Energy Office of Nuclear Energy under the Material Recovery and Waste Form Development Campaign within the Nuclear Fuel Cycle and Supply Chain Program. JL acknowledges the support of a DOE ARPA-E program under the award number of DEAR0001615. The authors would like to thank Miroslava Peterson (PNNL) for coordinating XCT testing and Joelle Reiser (PNNL) for peer reviewing the manuscript.

9 References

(1) Kroizman-Sheiner, E.; Brickner, D.; Canfi, A.; Schwarzfuchs, D. Blocking of the thyroid against I-131 following a nuclear disaster. *Harefuah* **2005**, *144*, 497.

(2) Zablotska, L. B.; Ron, E.; Rozhko, A. V.; Hatch, M.; Polyanskaya, O. N.; Brenner, A. V.; Lubin, J.; Romanov, G. N.; McConnell, R. J.; O'Kane, P.; Evseenko, V. V.; Drozdovitch, V. V.; Luckyanov, N.; Minenko, V. F.; Bouville, A.; Masyakin, V. B. Thyroid cancer risk in Belarus among children and adolescents exposed to radioiodine after the Chornobyl accident. *British J. Cancer* **2011**, *104*, 181.

(3) Tokonami, S.; Hosoda, M.; Akiba, S.; Sorimachi, A.; Kashiwakura, I.; Balonov, M. Thyroid doses for evacuees from the Fukushima nuclear accident. *Sci. Rep.* **2012**, *2*, 507.

(4) Pénélope, R.; Campayo, L.; Fournier, M.; Gossard, A.; Grandjean, A. Solid sorbents for gaseous iodine capture and their conversion into stable waste forms. *J. Nucl. Mater.* **2022**, *563*, 153635.

(5) Tesfay Reda, A.; Pan, M.; Zhang, D.; Xu, X. Bismuth-based materials for iodine capture and storage: A review. *J. Environ. Chem. Eng.* **2021**, *9*, 105279.

(6) Robshaw, T. J.; Turner, J.; Kearney, S.; Walkley, B.; Sharrad, C. A.; Ogden, M. D. Capture of aqueous radioiodine species by metallated adsorbents from wastestreams of the nuclear power industry: a review. *SN Appl. Sci.* **2021**, *3*, 843.

(7) Riley, B. J.; Vienna, J. D.; Strachan, D. M.; McCloy, J. S.; Jerden Jr, J. L. Materials and processes for the effective capture and immobilization of radioiodine: A review. *J. Nucl. Mater.* **2016**, *470*, 307.

(8) Nandanwar, S. U.; Coldsnow, K.; Utgikar, V.; Sabharwall, P.; Eric Aston, D. Capture of harmful radioactive contaminants from off-gas stream using porous solid sorbents for clean environment – A review. *Chem. Eng. J.* **2016**, *306*, 369.

(9) Haefner, D. R.; Tranter, T. J. *Methods of Gas Phase Capture of Iodine from Fuel Reprocessing Off-Gas: A Literature Survey*, INL/EXT-07-12299, Idaho National Laboratory, Idaho Falls, ID, 2007.

(10) Reiser, J. T.; Lawter, A. R.; Avalos, N. A.; Bonnett, J.; Riley, B. J.; Chong, S.; Canfield, N.; Saslow, S. A.; Bourchy, A.; Asmussen, R. M. Review and experimental comparison of the durability of iodine waste forms in semi-dynamic leach testing. *Chem. Eng. J. Adv.* **2022**, *11*, 100300.

(11) Asmussen, R. M.; Turner, J.; Chong, S.; Riley, B. J. Review of recent developments in iodine wasteform production. *Front. Chem.* **2022**, *10*, 1043653.

(12) Asmussen, R. M.; Matyáš, J.; Qafoku, N. P.; Kruger, A. A. Silver-functionalized silica aerogels and their application in the removal of iodine from aqueous environments. *J. Haz. Mater.* **2019**, *379*, 119364.

(13) Asmussen, R. M.; Ryan, J. V.; Matyas, J.; Crum, J. V.; Reiser, J. T.; Avalos, N.; McElroy, E. M.; Lawter, A. R.; Canfield, N. C. Investigating the Durability of Iodine Waste Forms in Dilute Conditions. *Mater.* **2019**, *12*, 686.

(14) 261, F. R. C. In *Federal Regulation 40 CFR 261*; Agency, E. P., Ed.; Environmental Protection Agency.

(15) Riley, B. J.; Kroll, J. O.; Peterson, J. A.; Matyáš, J.; Olszta, M. J.; Li, X.; Vienna, J. D. Silver-loaded aluminosilicate aerogels as iodine sorbents. *ACS Appl. Mater. Interfaces* **2017**, *9*, 32907.

(16) Riley, B. J.; Chong, S.; Beck, C. L. Iodine vapor reactions with pure metal wires at temperatures of 100-139 °C in air. *Ind. Eng. Chem. Res.* **2021**, *60*, 17162.

(17) Bruffey, S. H.; Jordan, J. A.; Jubin, R. T.; Parks, M. L.; Watkins, T. R. *Hot Isostatic Pressing of Engineered Forms of I-AgZ*, NTRD-MRWFD-2017-000412, ORNL/SR-2017/707, Oak Ridge National Laboratory, Oak Ridge, TN, 2017.

(18) Riley, B. J.; Chong, S.; Olszta, M. J.; Peterson, J. A. Evaluation of getter metals in Na-Al-Si-O aerogels and xerogels for the capture of iodine gas. *ACS Appl. Mater. Interfaces* **2020**, *12*, 19682.

(19) Cordova, E. A.; Garayburu-Caruso, V.; Pearce, C. I.; Cantrell, K. J.; Morad, J. W.; Gillispie, E. C.; Riley, B. J.; Colon, F. C.; Levitskaia, T. G.; Saslow, S. A.; Qafoku, O.; Resch, C. T.; Rigali, M. J.; Szecsody, J. E.; Heald, S. M.; Balasubramanian, M.; Meyers, P.; Freedman, V. L. Hybrid sorbents for ^{129}I capture from contaminated groundwater. *ACS Appl. Mater. Interfaces* **2020**, *12*, 26113.

(20) Yu, Q.; Jiang, X.; Cheng, Z.; Liao, Y.; Pu, Q.; Duan, M. Millimeter-sized Bi_2S_3@polyacrylonitrile hybrid beads for highly efficient iodine capture. *New J. Chem.* **2020**, *44*, 16759.

(21) Matyáš, J.; Ilton, E. S.; Lahiri, N.; Li, X. S.; Silverstein, J. A. *Bismuth-Functionalized Silica Aerogels for Iodine Capture*, PNNL-32086, Pacific Northwest National Laboratory, Richland, WA, 2021.

(22) Tian, Z.; Chee, T.-S.; Zhang, X.; Lei, L.; Xiao, C. Novel bismuth-based electrospinning materials for highly efficient capture of radioiodine. *Chem. Eng. J.* **2021**, *412*, 128687.

(23) Tian, Z.; Chee, T.-S.; Zhu, L.; Duan, T.; Zhang, X.; Lei, L.; Xiao, C. Comprehensive comparison of bismuth and silver functionalized nickel foam composites in capturing radioactive gaseous iodine. *J. Haz. Mater.* **2021**, *417*, 125978.

(24) Baskaran, K.; Ali, M.; Riley, B. J.; Zharov, I.; Carlson, K. Evaluating the physisorption and chemisorption of iodine on bismuth-functionalized carbon foams. *ACS Mater. Lett.* **2022**, *4*, 1780.

(25) Vance, E. R.; Grant, C.; Karatchevtseva, I.; Aly, Z.; Stopic, A.; Harrison, J.; Thorogood, G.; Wong, H.; Gregg, D. J. Immobilization of iodine via copper iodide. *J. Nucl. Mater.* **2018**, *505*, 143.

(26) Zhou, J.; Chen, Q.; Li, T.; Lan, T.; Bai, P.; Liu, F.; Yuan, Z.; Zheng, W.; Yan, W.; Yan, T. Porous Copper-Loaded Zeolites for High-Efficiency Capture of Iodine from Spent Fuel Reprocessing Off-Gas. *Inorg. Chem.* **2022**, *61*, 7746.

(27) Riley, B. J.; Pierce, D., A; Chun, J.; Matyáš, J.; Lepry, W. C.; Garn, T.; Law, J.; Kanatzidis, M. G. Polyacrylonitrile-chalcogel hybrid sorbents for radioiodine capture. *Environ. Sci. Technol.* **2014**, *48*, 5832.

(28) Riley, B. J.; Pierce, D. A.; Lepry, W. C.; Kroll, J. O.; Chun, J.; Subrahmanyam, K. S.; Kanatzidis, M. G.; Alblouwy, F. K.; Bulbule, A.; Sabolsky, E. M. Consolidation of Tin Sulfide Chalcogels and Xerogels with and without Adsorbed Iodine. *Ind. Eng. Chem. Res.* **2015**, *54*, 11259.

(29) Yang, J. H.; Cho, Y.-J.; Shin, J. M.; Yim, M.-S. Bismuth-embedded SBA-15 mesoporous silica for radioactive iodine capture and stable storage. *J. Nucl. Mater.* **2015**, *465*, 556.

(30) Klimakov, A. M.; Popovkin, B. A.; Novoselova, A. V. T-X projection of structural diagrams of BiL_3-Bi_2O_3 system. *Russ. J. Inorg. Chem.* **1974**, *19*, 2553.

(31) Liu, L.; Liu, W.; Zhao, X.; Chen, D.; Cai, R.; Yang, W.; Komarneni, S.; Yang, D. Selective Capture of Iodide from Solutions by Microrosette-like δ-Bi_2O_3. *ACS Appl. Mater. Interfaces* **2014**, *6*, 16082.

(32) ASTM *ASTM C1308-21, Standard Test Method for Accelerated Leach Test for Measuring Contaminant Releases From Solidified Waste*, ASTM C1308-21, American Society for Testing and Materials International, ASTM International Book of Standards Volume 12.01, West Conshohocken, PA, 2021.

(33) Gattu, V. K.; Stariha, S.; Lee, E.; Fortner, J. A.; Ebert, W. L. *Degradation Tests with Iodide Waste Forms: FY20 Status Report*, ANL/CFCT-20/22, Argonne National Laboratory, Lemont, IL, 2020.

(34) Stariha, S. A.; Gattu, V. K.; Ebert, W. L. *Durability Tests with Iodide Waste Form Materials*, ANL/CFCT-22/50, Argonne National Laboratory, Lemont, IL, 2022.

(35) Bruffey, S. H.; Jubin, R. T. *Recommend HIP Conditions for AgZ*, FCRD-MRWFD-2015-000423, ORNL/SPR-2015/503, Oak Ridge National Laboratory, Oak Ridge, TN, 2015.

(36) Maddrell, E. R.; Vance, E. R.; Grant, C.; Aly, Z.; Stopic, A.; Palmer, T.; Harrison, J.; Gregg, D. J. Silver iodide sodalite – Wasteform / Hip canister interactions and aqueous durability. *J. Nucl. Mater.* **2019**, *517*, 71.

(37) Vance, E. R.; Perera, D. S.; Moricca, S.; Aly, Z.; Begg, B. D. Immobilisation of ^{129}I by encapsulation in tin by hot-pressing at 200°C. *J. Nucl. Mater.* **2005**, *341*, 93.

(38) Riley, B. J.; Chong, S.; Zhao, M.; Lian, J. Densification and Immobilization of AgI-Containing Iodine Waste Forms Using Spark Plasma Sintering. *Ind. Eng. Chem. Res.* **2023**, *62*, 8779.

(39) Yang, J. H.; Shin, J. M.; Park, J. J.; Park, G. I. Waste Form of Silver Iodide (AgI) with Low-Temperature Sintering Glasses. *Sep. Sci. Technol.* **2014**, *49*, 298.

(40) Yang, J. H.; Park, H.-S.; Cho, Y.-Z. Al_2O_3-containing silver phosphate glasses as hosting matrices for radioactive iodine. *J. Nucl. Sci. Technol.* **2017**, *54*, 1330.

(41) Saslow, S. A.; Snyder, M. M. V.; Williams, B.; Asmussen, R. M.; Baum, S.; Leavy, I. I.; Varga, T. *Leach Testing of Laboratory-Scale Melter Evaporator Condensate Cementitious Waste Forms*, PNNL-28917, Pacific Northwest National Laboratory, Richland, WA, 2019.

(42) Lide, D. R. *CRC Handbook of Chemistry and Physics*; 88th ed.; CRC Press: Boca Raton, FL, 2008.

(43) Wagner, B.; Huttner, A.; Bischof, D.; Engel, A.; Witte, G.; Heine, J. Chemical Surface Reactivity and Morphological Changes of Bismuth Triiodide (BiI_3) under Different Environmental Conditions. *Langmuir* **2020**, *36*, 6458.

(44) Sajjad, M.; Singh, N.; Larsson, J. A. Bulk and monolayer bismuth oxyiodide (BiOI): Excellent high temperature p-type thermoelectric materials. *AIP Adv.* **2020**, *10*, 075309.

(45) ASTM *ASTM C1285-21, Standard Test Methods for Determining Chemical Durability of Nuclear, Hazardous, and Mixed Waste Glasses and Multiphase Glass Ceramics: The Product Consistency Test (PCT)*, ASTM C1285-21, American Society for Testing and Materials International, ASTM International Book of Standards Volume 12.01, West Conshohocken, PA, 2021.

(46) Lanzetta, L.; Webb, T.; Zibouche, N.; Liang, X.; Ding, D.; Min, G.; Westbrook, R. J. E.; Gaggio, B.; Macdonald, T. J.; Islam, M. S.; Haque, S. A. Degradation mechanism of hybrid tin-based perovskite solar cells and the critical role of tin (IV) iodide. *Nat. Commun.* **2021**, *12*, 2853.

(47) Zhu, W.; Xin, G.; Scott, S. M.; Xu, W.; Yao, T.; Gong, B.; Wang, Y.; Li, M.; Lian, J. Deciphering the degradation mechanism of the lead-free all inorganic perovskite Cs_2SnI_6. *npj Mater. Degrad.* **2019**, *3*, 7.

(48) Yang, K.; Wang, Y.; Shen, J.; Scott, S. M.; Riley, B. J.; Vienna, J. D.; Lian, J. $Cs_3Bi_2I_9$-hydroxyapatite composite waste forms for cesium and iodine immobilization. *J. Adv. Ceram.* **2022**, *11*, 712.

(49) Sui, Y.; Fu, W.; Yang, H.; Zeng, Y.; Zhang, Y.; Zhao, Q.; Li, Y.; Zhou, X.; Leng, Y.; Li, M.; Zou, G. Low Temperature Synthesis of Cu_2O Crystals: Shape Evolution and Growth Mechanism. *Cryst. Growth Des.* **2010**, *10*, 99.

(50) Su, J.; Xiao, Y.; Ren, M. Direct hydrolysis synthesis of BiOI flowerlike hierarchical structures and it's photocatalytic activity under simulated sunlight irradiation. *Catalys. Comm.* **2014**, *45*, 30.

(51) Luz, A.; Feldmann, C. Phase-transfer assisted synthesis of BiOI nanoplatelets, quantum-confined color and selective modification of surface conditioning. *Solid State Ionics* **2011**, *13*, 1017.

(52) Bartolomé, J.; Climent-Pascual, E.; Redondo-Obispo, C.; Zaldo, C.; Álvarez, Á. L.; de Andrés, A.; Coya, C. Huge Photostability Enhancement in Bismuth-Doped Methylammonium Lead Iodide Hybrid Perovskites by Light-Induced Transformation. *Chem. Mater* **2019**, *31*, 3662.

(53) Crovetto, A.; Hajijafarassar, A.; Hansen, O.; Seger, B.; Chorkendorff, I.; Vesborg, P. C. K. Parallel Evaluation of the BiI_3, BiOI, and Ag_3BiI_6 Layered Photoabsorbers. *Chem. Mater.* **2020**, *32*, 3385.

(54) Lere-Adams, A. J.; Dixon Wilkins, M. C.; Bollinger, D.; Stariha, S.; Farzana, R.; Dayal, P.; Gregg, D. J.; Chong, S.; Riley, B. J.; Heiden, Z. M.; McCloy, J. S. Glass-bonded ceramic waste forms for immobilization of radioiodine from caustic scrubber wastes. *J. Nucl. Mater.* **2024**, *591*, 154938.

(55) Riley, B. J.; McFarlane, J.; DelCul, G. D.; Vienna, J. D.; Contescu, C. I.; Forsberg, C. W. Molten salt reactor waste and effluent management strategies: A review. *Nucl. Eng. Des.* **2019**, *345*, 94.

(56) Andrews, H. B.; McFarlane, J.; Chapel, A. S.; Ezell, N. D. B.; Holcomb, D. E.; de Wet, D.; Greenwood, M. S.; Myhre, K. G.; Bryan, S. A.; Lines, A.; Riley, B. J.; Felmy, H. M.; Humrickhouse, P. W. Review of molten salt reactor off-gas management considerations. *Nucl. Eng. Des.* **2021**, *385*, 111529.

(57) Riley, B. J.; Turner, J.; McFarlane, J.; Chong, S.; Carlson, K.; Matyas, J. Iodine solid sorbent design: A literature review of the critical criteria for consideration. *Mater. Adv.* **2024**.

10 Supporting Information

11 Sample Information

Table S1. Information for starting chemicals used for experiments in this study. CAS denotes Chemical Abstract Service (CAS) Registry Number.

Chemical	Purity	Brand	CAS#
AgI	99.999%	Alfa Aesar	7783-96-2
BiI_3	99.999%	Thermo Scientific	7787-64-6
BiOI	98+%	Alfa Aesar	7787-63-5
CuI	99.999%	Thermo Scientific	7681-65-4
SnI_4	95%	Thermo Scientific	7790-47-8

12 TGA Parameters

Table S2. Heating profile for TGA analysis. All measurements were performed under argon. All heating rates (r_H) were 10 °C·min^{-1}. "RT" denotes room temperature.

Sample	Heating profile	Isothermal hold
AgI	RT–500°C	500 °C (5.0 min)
BiI_3	RT–350°C	–
BiOI	RT–700°C	700 °C (5.0 min)
CuI	RT–550°C	–
SnI_4	RT–100°C	100 °C (5.0 min)

13 Post-SPS Measurements on Pellets

Table S3. Approximate green pellet masses (m_p) as well as pellet density measurements (ρ_{meas}) after SPS processing. Note that the differences in density values between reference ($\rho_{b,t}$) and ρ_{meas} values is, at least in part, due to the formation of other crystalline phases in the samples during the SPS processing (e.g., SnI_2 formation for the SnI_4 pellet). These phases can be seen in the XRD analysis data. In some cases, multiple ρ_{meas} values are shown.

Sample	m_p (g)	$\rho_{b,t}$ (g·cm^{-3})	ρ_{meas} (g·cm^{-3})
AgI	0.321	5.675	5.662, 5.618
BiI_3	0.326	5.780	5.638
BiOI	0.448	7.92	7.58
CuI	0.321	5.670	5.353
SnI_4	0.258	4.56	5.67

14 OM/SEM/EDS

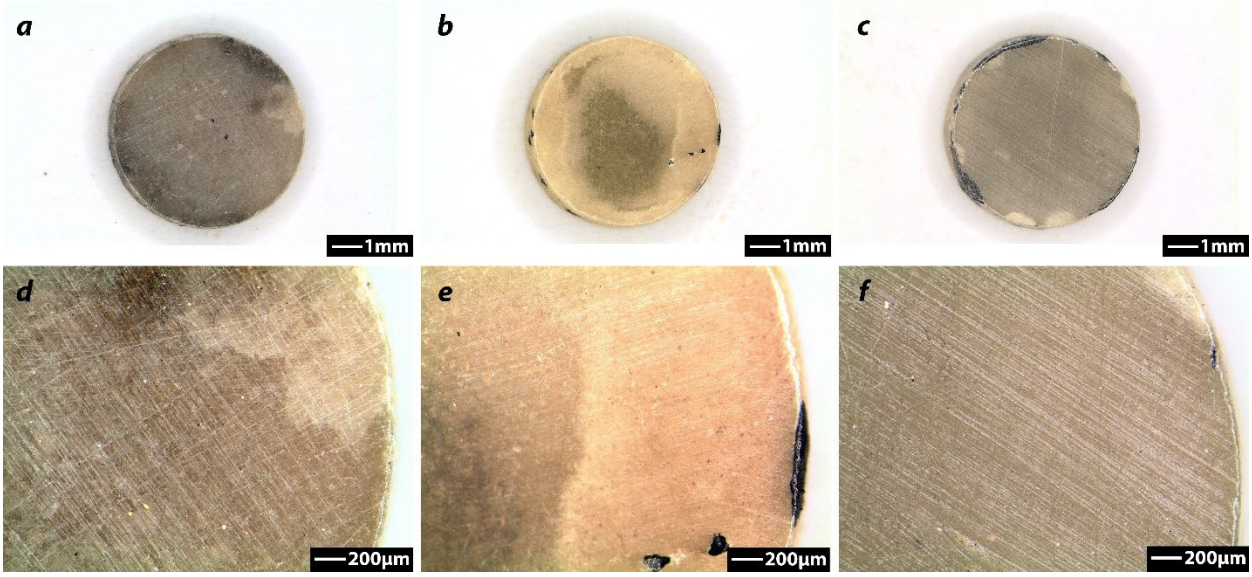

Figure S1. Optical micrographs of the SPS-processed AgI pellets, including (a-c) low-magnification (1×) images so the entire pellet could be observed and images and (d-f) higher magnification (5×) images to provide more details.

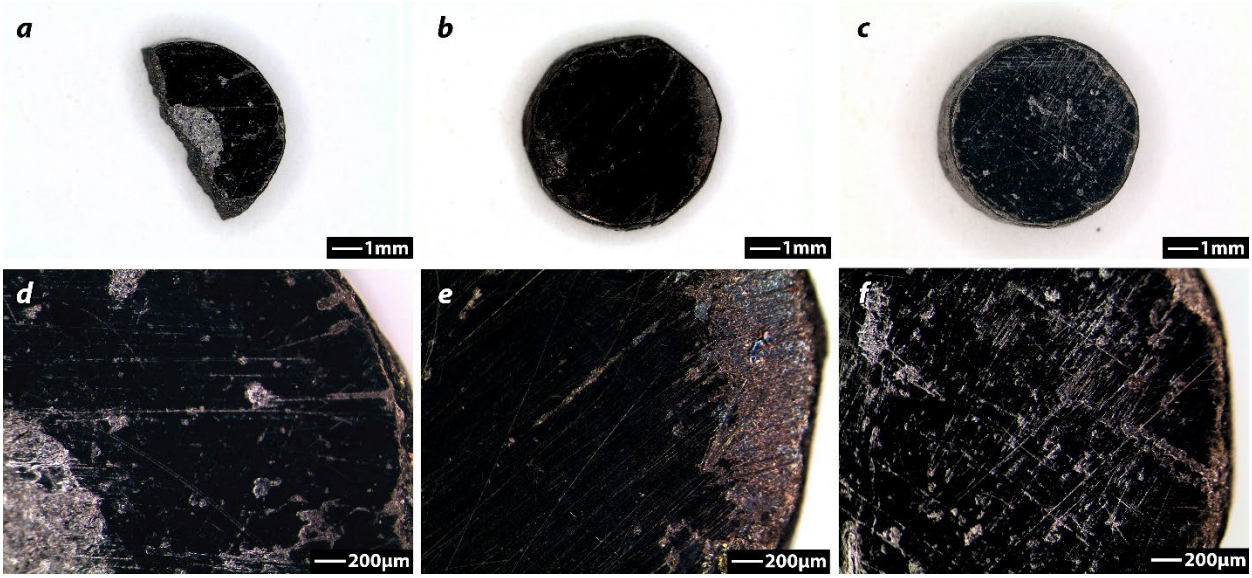

Figure S2. Optical micrographs of the SPS-processed BiI_3 pellets, including (a-c) low-magnification (1×) images so the entire pellet could be observed and images and (d-f) higher magnification (5×) images to provide more details.

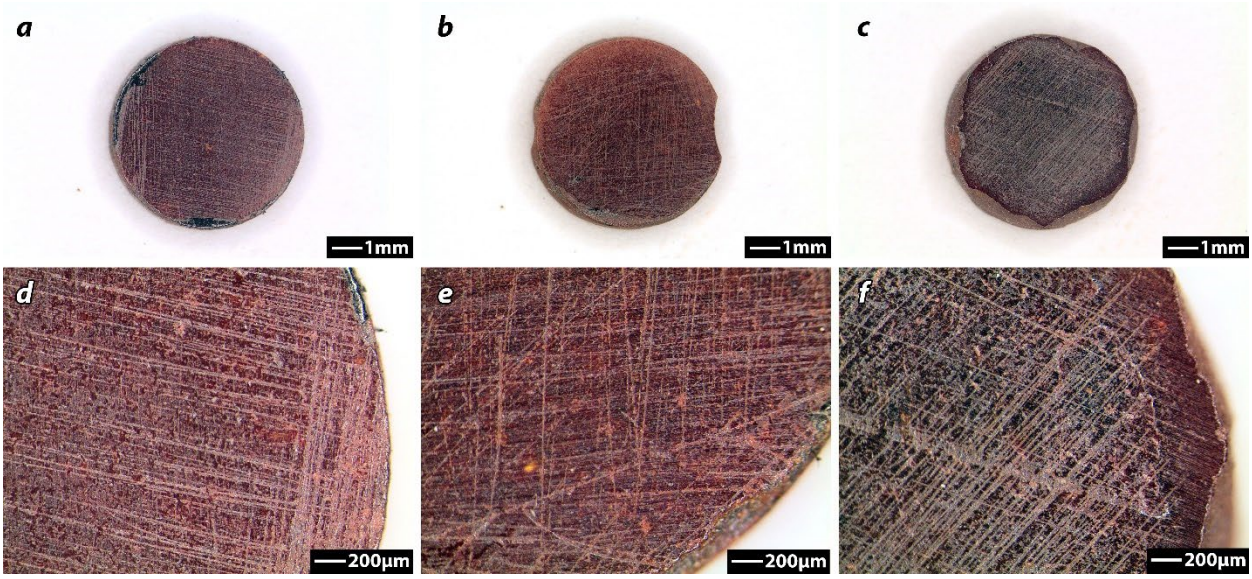

Figure S3. Optical micrographs of the SPS-processed BiOI pellets, including (a-c) low-magnification (1×) images so the entire pellet could be observed and images and (d-f) higher magnification (5×) images to provide more details.

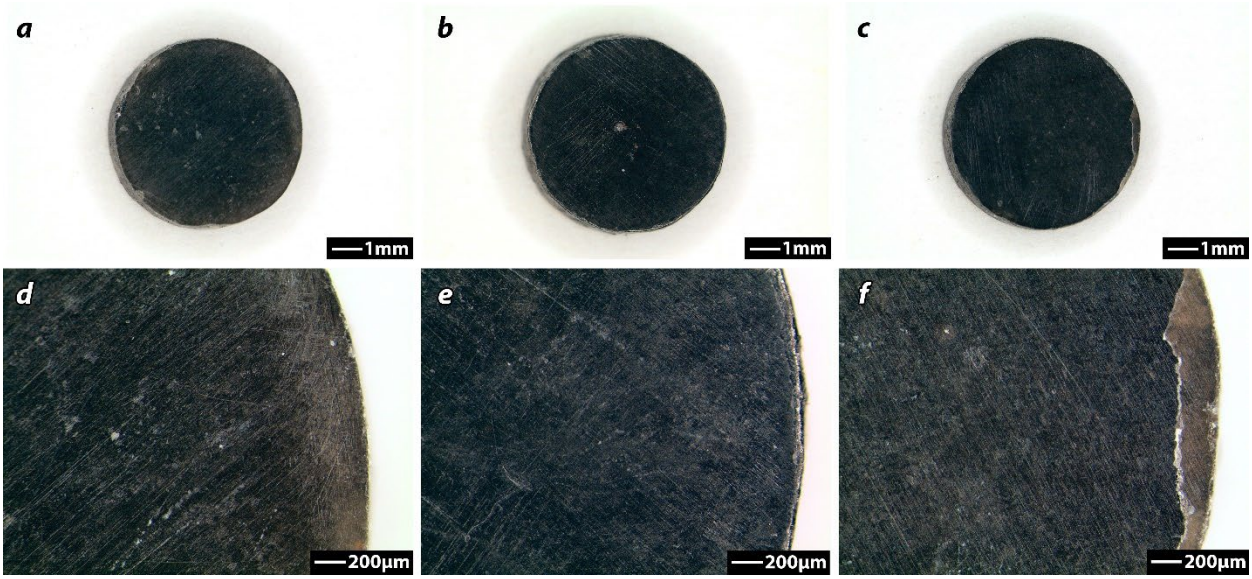

Figure S4. Optical micrographs of the SPS-processed CuI pellets, including (a-c) low-magnification (1×) images so the entire pellet could be observed and images and (d-f) higher magnification (5×) images to provide more details.

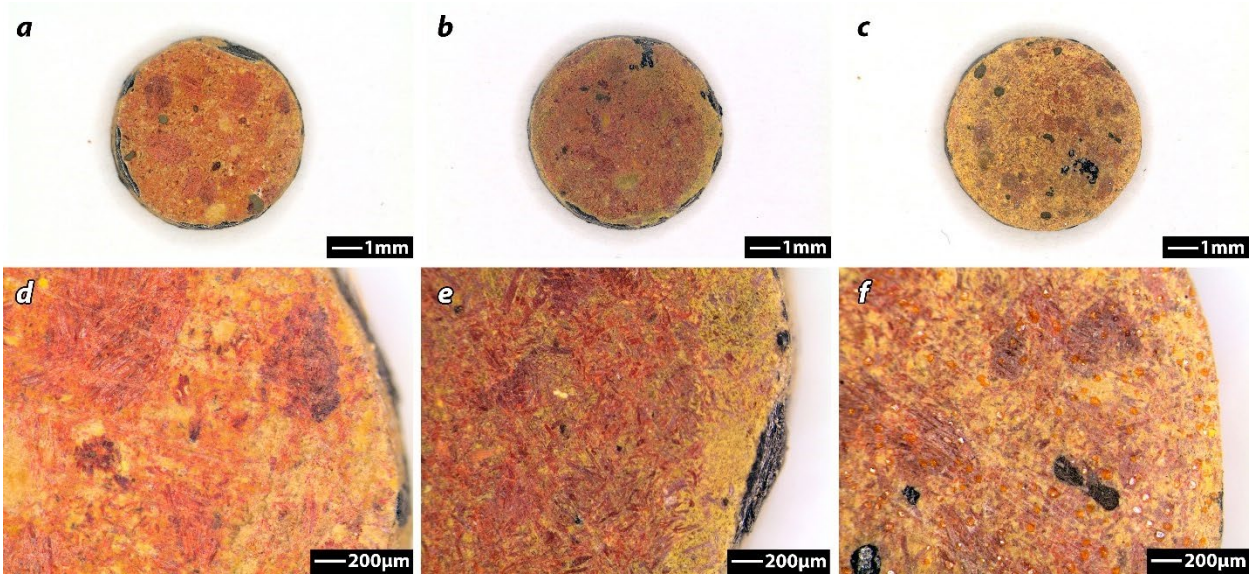

Figure S5. OM of the SPS-processed SnI_4 pellets, including (a-c) low-magnification (1×) images so the entire pellet could be observed and images and (d-f) higher magnification (5×) images to provide more details.

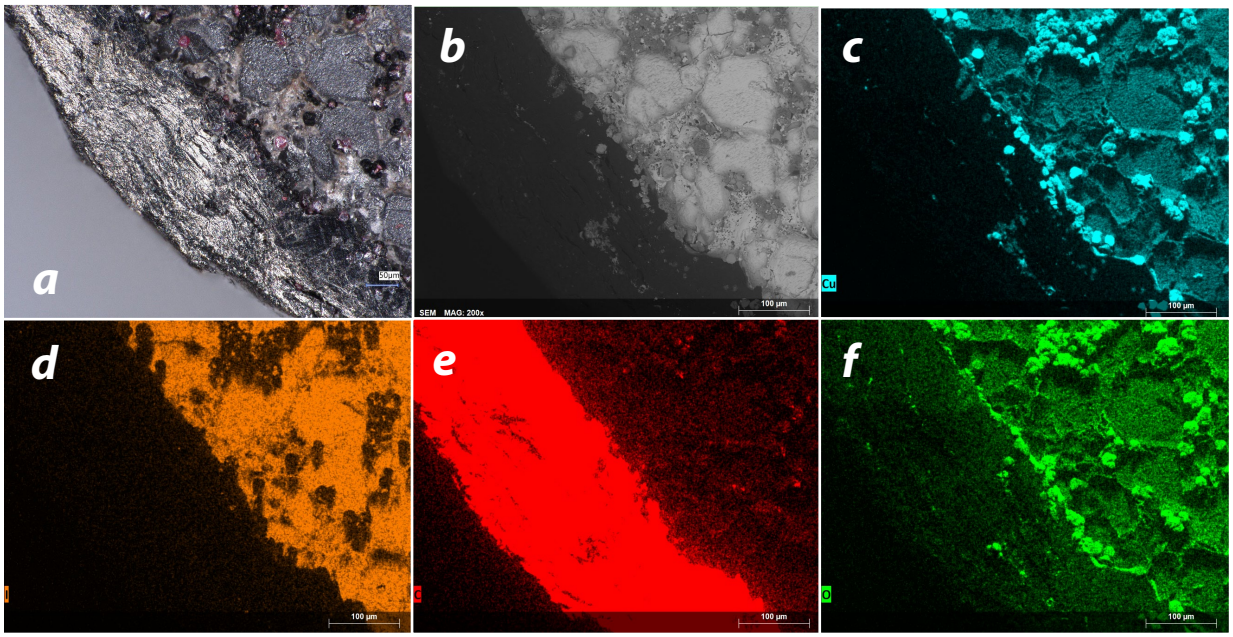

Figure S6. Images of the edge of the CuI-U specimen post-leach testing, including (a) OM taken at 500×, (b) SEM micrograph at 200×, (c) EDS map of Cu, (d) EDS map of I, (e) EDS map of C, (f) EDS map of O.

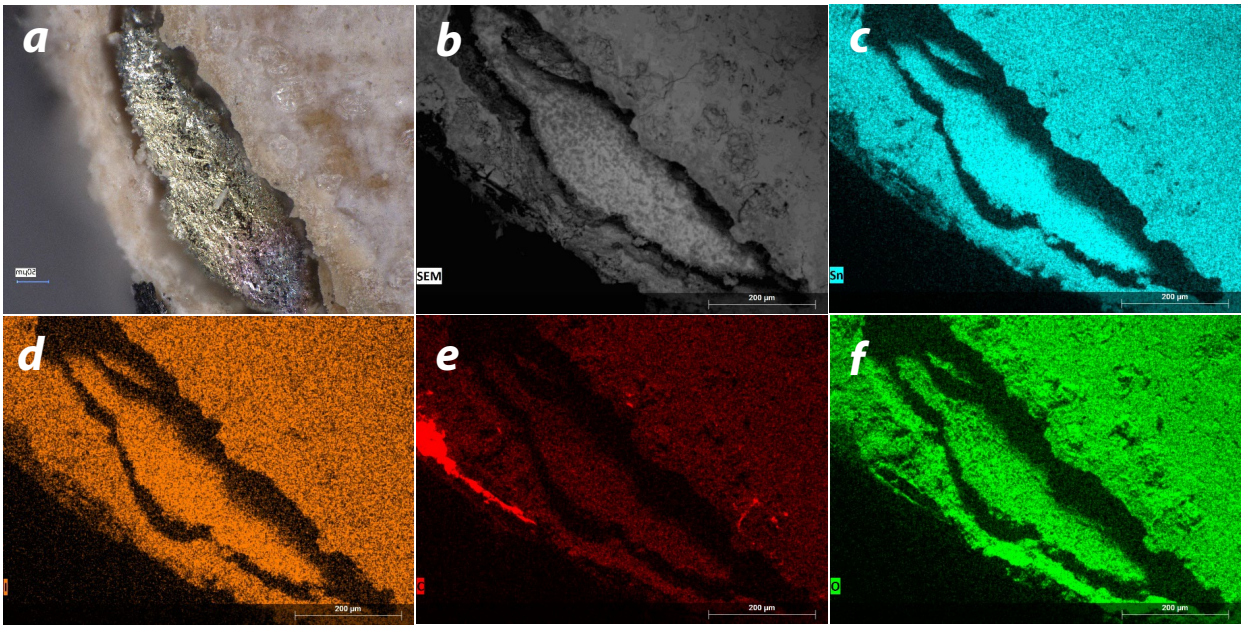

Figure S7. Images of the edge of the SnI_4-U specimen post-leach testing, including (a) OM taken at 500×, (b) SEM micrograph at 200×, (c) EDS map of Sn, (d) EDS map of I, (e) EDS map of C, and (f) EDS map of O.

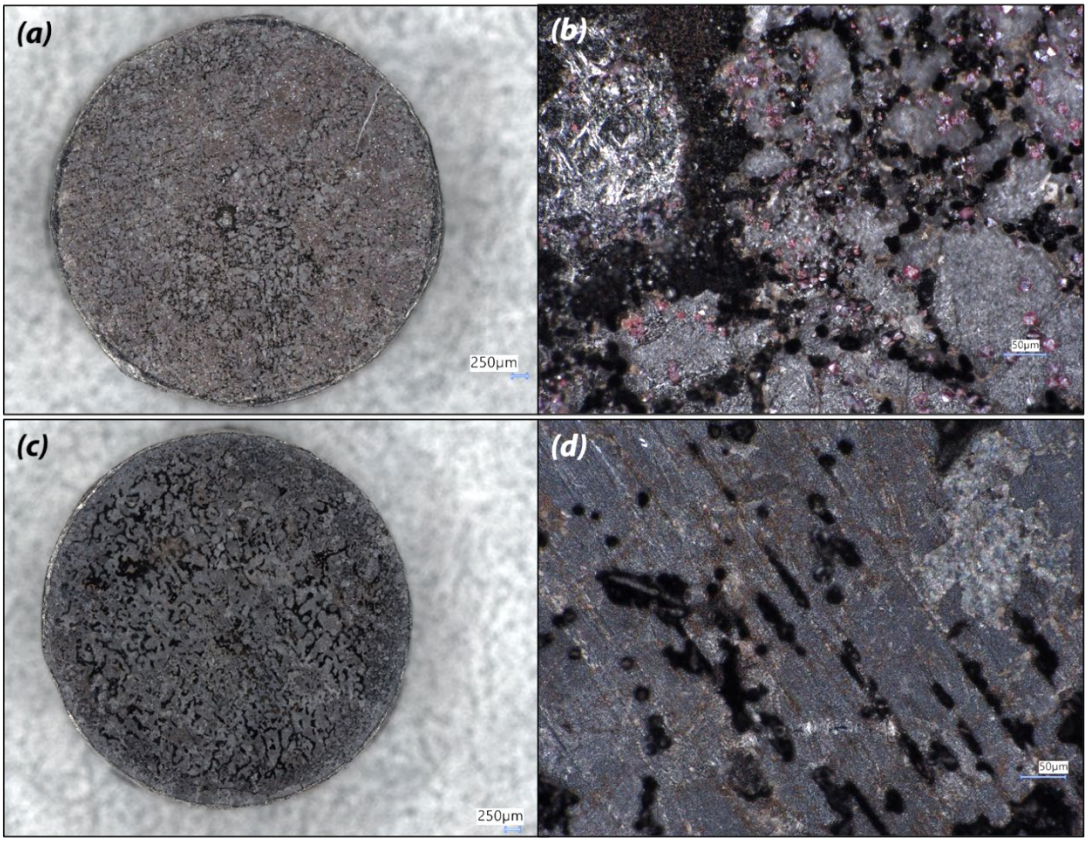

Figure S8. OM of the CuI-U specimen, representing both circular faces of the sample, including (a) Face #1 at 100×, (b) Face #1 at 500×, (c) Face #2 at 100×, and (d) Face #2 at 500×. The dark red crystals that can be seen in part (b) are identified as Cu_2O.

Table S4. EDS spot analysis data for the BiI_3-U sample with analysis locations shown in Figure S9 with averages and standard deviations (SD) shown at the bottom of each dataset.

Shell of sample			
Spectrum	Oxygen	Iodine	Bismuth
Spectrum 1	23.14	39.41	37.45
Spectrum 2	19.66	40.78	39.55
Spectrum 3	17.48	44.19	38.33
Spectrum 4	23.16	40.96	35.89
Spectrum 5	17.38	43.41	39.21
Spectrum 6	17.33	45.12	37.54
Spectrum 7	16.83	45.56	37.61
Spectrum 8	20.50	39.24	40.25
Mean	**19.44**	**42.33**	**38.23**
SD	**2.62**	**2.54**	**1.40**

Core of sample			
Spectrum	Oxygen	Iodine	Bismuth
Spectrum 9	8.57	63.77	27.66
Spectrum 10	4.22	68.54	27.25
Spectrum 11	5.21	66.28	28.51
Spectrum 12	5.91	66.02	28.07
Spectrum 13	7.67	65.56	26.77
Spectrum 14	4.00	68.30	27.70
Spectrum 15	4.80	67.36	27.83
Spectrum 16	3.37	67.83	28.80
Mean	**5.47**	**66.71**	**27.82**
SD	**1.82**	**1.61**	**0.65**

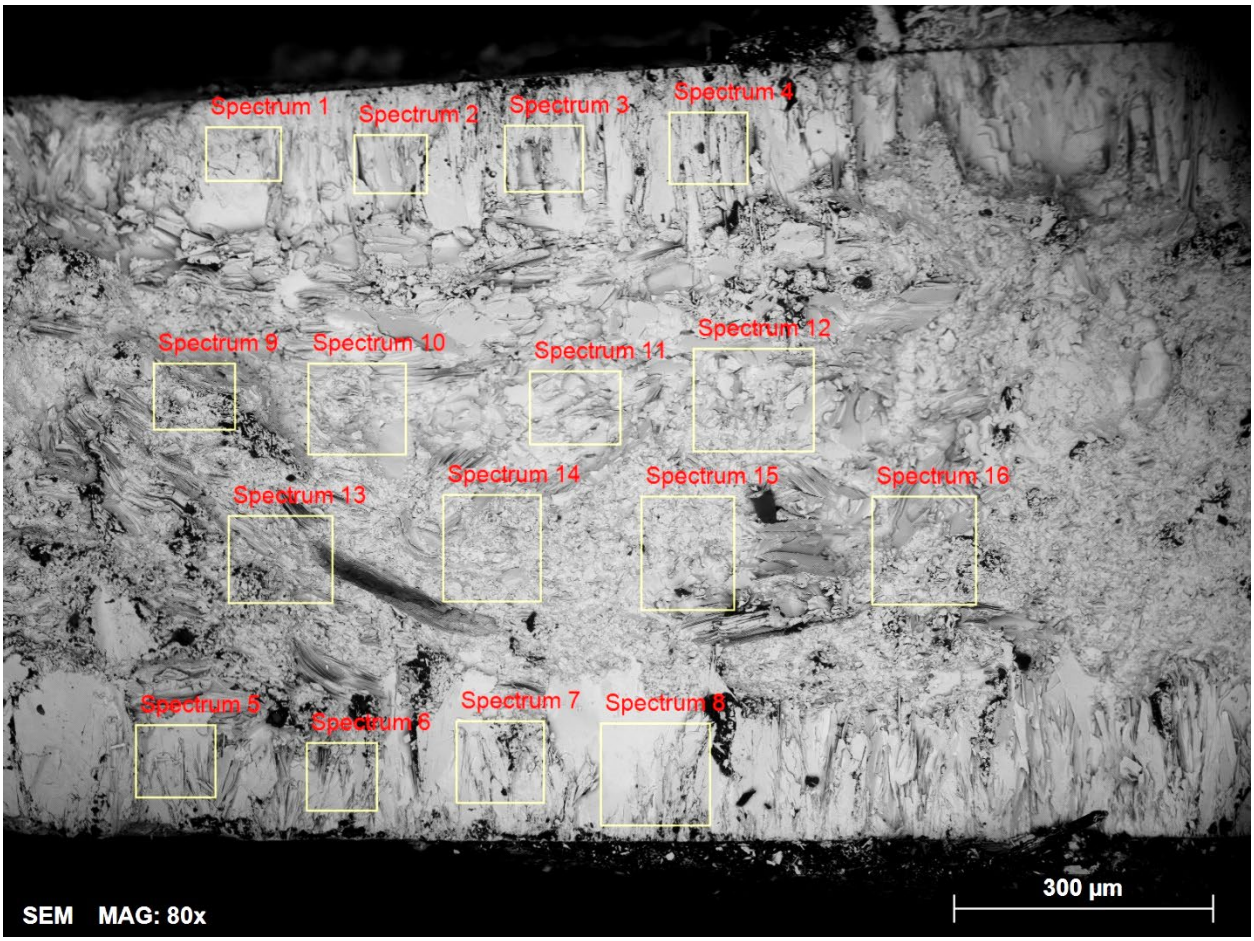

Figure S9. SEM micrograph and EDS spot locations for BiI_3-U sample discussed within the paper (see Figure 7) where data are presented above in Table S4.

15 XRD data

Table S5. Summary of XRD analysis data.

Sample	Pellets	Phases	Comments
AgI	AgI-1	AgI (hex, cubic), Ag	Ag phase shown only on the 1st pellet
	AgI-2	AgI (hex, cubic)	
	AgI-3	AgI (hex, cubic)	
BiI_3	BiI_3-1	BiI_3	Small humps at 30° 2θ and 32° 2θ might be BiOI, but too small to confirm
	BiI_3-2	BiI_3	
	BiI_3-3	BiI_3	
BiOI	BiOI-1	BiOI, graphite	Peak at ~27° 2θ seems to be graphite; peak at ~29° 2θ is not identified. Maybe $Bi_2O_{2.33}$, but more investigation is needed.
	BiOI-2	BiOI, graphite	
	BiOI-3	BiOI, graphite	
CuI	CuI-1	CuI	Peak at ~27° 2θ seems to be graphite (residual from the SPS process)
	CuI-2	CuI	
	CuI-3	CuI	
SnI_4	SnI_4-1	SnI_4, SnI_2	N/A
	SnI_4-2	SnI_4, SnI_2	
	SnI_4-3	SnI_4, SnI_2	

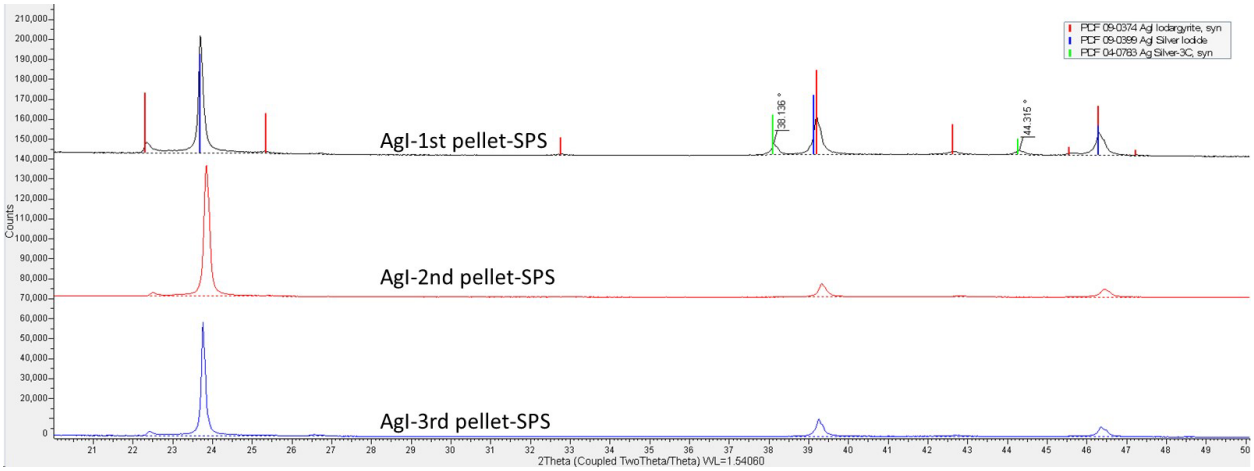

Figure S10. XRD data for AgI pellets.

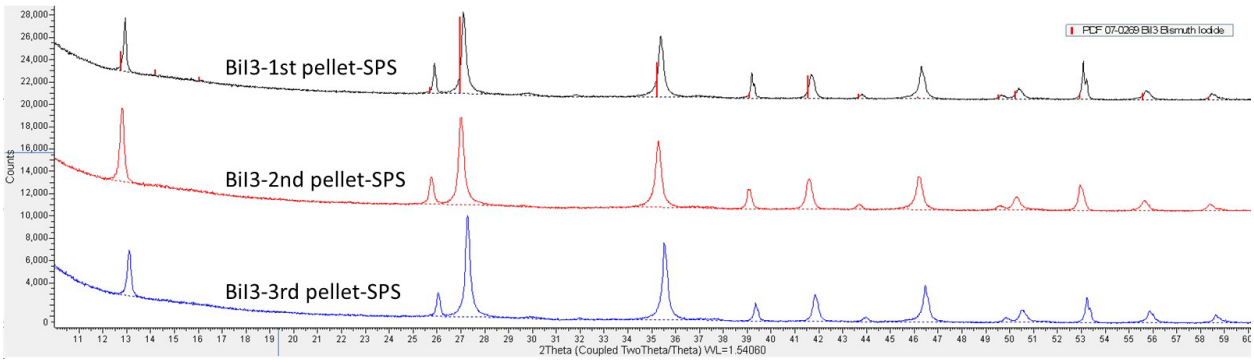

Figure S11. XRD data for BiI_3 pellets.

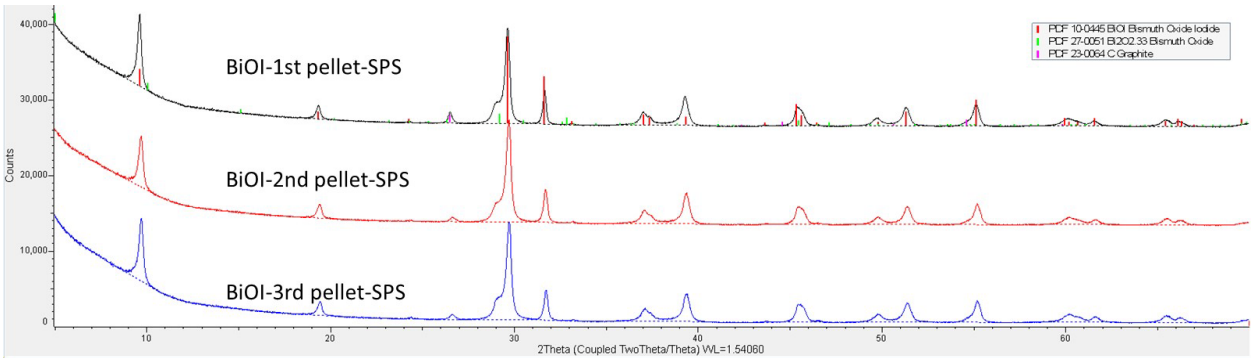

Figure S12. XRD data for BiOI pellets.

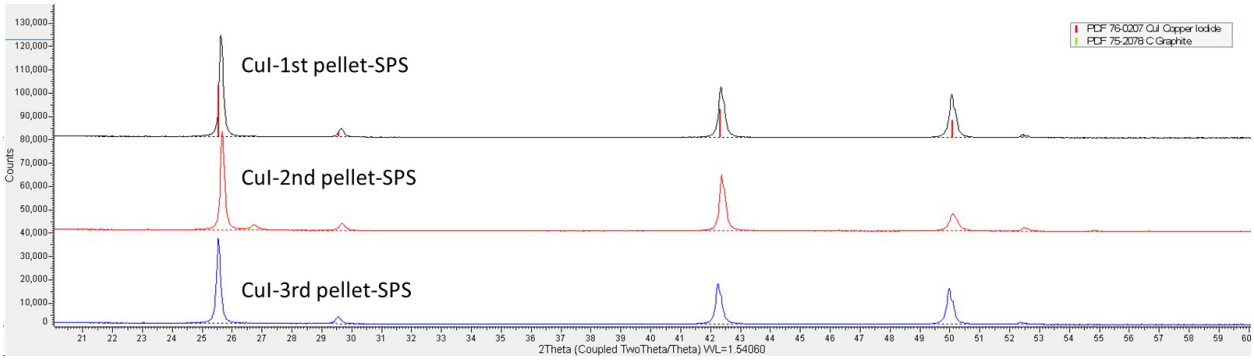

Figure S13. XRD data for CuI pellets.

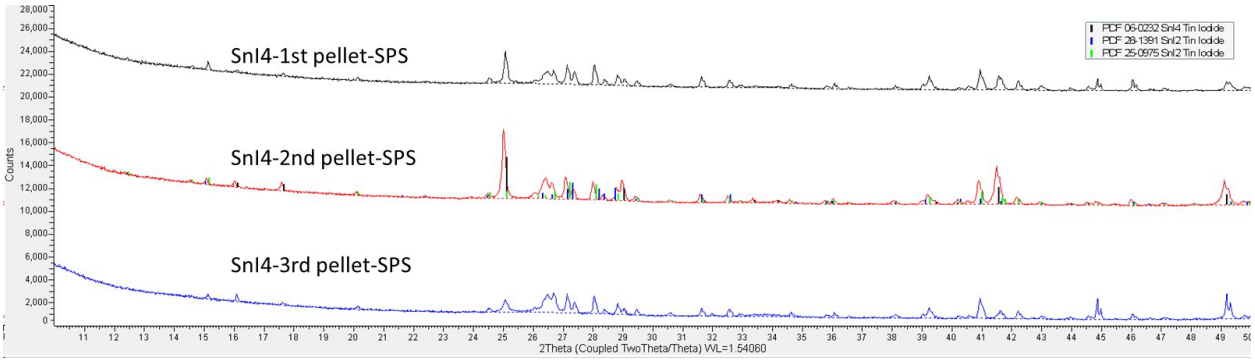

Figure S14. XRD data for SnI_4 pellets.

16 Chemical Durability Testing Data

Table S6. Cumulative fraction leached ($CFL_{N[^{127}I]}$ in g·g^{-1}) values in the "U" SPS specimens. R^2 represents the Pearson Correlation Coefficient for the data over the first four days of the tests.

Day	AgI-U	BiI_3-U	BiOI-U	CuI-U	SnI_4-U
1	4.22E-05	1.68E-01	1.36E-02	3.22E-03	9.70E-01
2	4.90E-05	2.10E-01	1.43E-02	6.82E-03	1.02E+00
3	5.56E-05	2.38E-01	1.47E-02	8.59E-03	1.03E+00
4	6.08E-05	2.49E-01	1.51E-02	9.96E-03	1.03E+00
7	6.86E-05	3.11E-01	1.59E-02	1.27E-02	1.04E+00
R^2 (D1-4)	1.00	0.94	0.98	0.95	0.74

Table S7. Summary of $NL_{[i]}$ data (g·m^{-2}) from "U" and "M" SPS coupons from the current study.

Analyte [i]	Sample ID	Time (Days)				
		1	2	3	4	7
[I]	AgI-M	0.0213	0.00207	0.00124	0.000530	0.00488
	AgI-U	0.0108	0.00171	0.00170	0.00132	0.00200
	BiI_3-M	8.77	1.76	1.17	0.542	0.651
	BiI_3-U	36.6	9.01	6.16	2.29	13.5
	BiOI-M	12.0	0.286	0.143	0.0693	0.126
	BiOI-U	3.67	0.186	0.121	0.105	0.216
	CuI-M	0.217	0.507	0.423	0.429	0.561
	CuI-U	0.934	1.04	0.513	0.399	0.789
	SnI_4-M	252	12.9	3.18	1.10	0.967
	SnI_4-U	126	6.42	0.809	0.503	1.34
[Cu]	CuI-M	0.475	0.474	0.406	0.391	0.821
	CuI-U	0.258	0.258	0.257	0.240	0.406
[Sn]	SnI_4-M	102	0.000	0.000	0.000	0.000
	SnI_4-U	2.70	0.000	0.000	0.000	0.000

Table S8. Normalized dissolution rates (*NDR*) as determined from data from an ASTM C1308 test of pellet specimens created in this study and in literature. This table was partially recreated from Reiser et al.[10] Here, HEBM refers to high-energy ball milling and CPS refers to cold-press and sinter.

Material	Sample Name	Consolidation Method	Iodine Loading (mass%)	Solution Exchange Time Intervals	*NDR* ($g \cdot m^{-2} \cdot d^{-1}$)
AgI	AgI-M	SPS	54.1%	Every 24 hrs from 1d-4d, then 7d	1.28E-03
AgI	AgI-U	SPS	54.1%	Every 24 hrs from 1d-4d, then 7d	1.59E-03
BiO_3	BiO_3-U	SPS	64.6%	Every 24 hrs from 1d-4d, then 7d	1.16E+00
BiO_3	BiO_3-M	SPS	64.6%	Every 24 hrs from 1d-4d, then 7d	5.86E+00
BiOI	BiOI-U	SPS	36.1%	Every 24 hrs from 1d-4d, then 7d	1.64E-01
BiOI	BiOI-M	SPS	36.1%	Every 24 hrs from 1d-4d, then 7d	1.36E-01
CuI	CuI-U	SPS	66.6%	Every 24 hrs from 1d-4d, then 7d	4.50E-01
CuI	CuI-M	SPS	66.6%	Every 24 hrs from 1d-4d, then 7d	6.38E-01
SnI_4	SnI_4-U	SPS	81.0%	Every 24 hrs from 1d-4d, then 7d	5.48E+00
SnI_4	SnI_4-M	SPS	81.0%	Every 24 hrs from 1d-4d, then 7d	2.40E+00
Iodoapatite	$Pb_{9.85}(VO_4)_6I_{1.7}$	HEBM/SPS	-	2 h, 5 h, 17 h, then every 24 h, up to ~25 days	2.3E-03
Glass-bonded iodosodalite	10N-750 (using 10% NBS-4 for GB); $SA \cdot V^{-1}$ of 8 m^{-1}	CPS	8% - 9%	Every 7d between 10d-24d	1.29E+00
Glass-bonded iodosodalite	10N-750 (using 10% NBS-4 for GB); $SA \cdot V^{-1}$ of 80 m^{-1}	CPS	8% - 9%	Every 7d between 10d-24d	1.7E-01
NaI iodosodalite	P40-10N-750C	CPS	13% – 19.8%	10d	7.7E-01
Pb iodovanadate	$Pb_{9.85}(VO_4)_6I_{1.7}$	HEBM/SPS	≈ 7%	7d	6.3E-03

Table S9. EQL values of ^{127}I as analyzed by ICP-MS and the metallic cation by ICP-OES.

Sample	Analyte	EQL (µg·L^{-1})	Sample	Analyte	EQL (µg·L^{-1})
Blank A-1d/2d	Iodine 127	0.730	CuI-M-4d	Iodine 127	365
Blank B-1d	Iodine 127	0.730	SnI4-M-4d	Iodine 127	730
Blank C-1d	Iodine 127	0.730	AgI-U-4d	Iodine 127	0.730
AgI-M-1d	Iodine 127	7.30	BiI3-U-4d	Iodine 127	730
BiI3-M-1d	Iodine 127	7300	BiOI-U-4d	Iodine 127	73.0
BiOI-M-1d	Iodine 127	7300	CuI-U-4d	Iodine 127	365
CuI-M-1d	Iodine 127	365	SnI4-U-4d	Iodine 127	365
SnI4-M-1d	Iodine 127	73000	Blank A-7d	Iodine 127	0.730
AgI-U-1d	Iodine 127	7.30	Blank B-7d	Iodine 127	0.730
BiI3-U-1d	Iodine 127	7300	Blank C-7d	Iodine 127	0.730
BiOI-U-1d	Iodine 127	730	AgI-M-7d	Iodine 127	0.730
CuI-U-1d	Iodine 127	365	BiI3-M-7d	Iodine 127	365
SnI4-U-1d	Iodine 127	73000	BiOI-M-7d	Iodine 127	73.0
Blank B-2d	Iodine 127	0.730	CuI-M-7d	Iodine 127	365
Blank C-2d	Iodine 127	0.730	SnI4-M-7d	Iodine 127	365
AgI-M-2d	Iodine 127	0.730	AgI-U-7d	Iodine 127	0.730
BiI3-M-2d	Iodine 127	730	BiI3-U-7d	Iodine 127	7300
BiOI-M-2d	Iodine 127	73.0	BiOI-U-7d	Iodine 127	73.0
CuI-M-2d	Iodine 127	365	CuI-U-7d	Iodine 127	730
SnI4-M-2d	Iodine 127	7300	SnI4-U-7d	Iodine 127	730
AgI-U-2d	Iodine 127	0.730	Blank A-1d/2d	Silver	1400
BiI3-U-2d	Iodine 127	7300	Blank B-1d	Silver	1400
BiOI-U-2d	Iodine 127	73.0	Blank C-1d	Silver	1400
CuI-U-2d	Iodine 127	730	AgI-M-1d	Silver	1400
SnI4-U-2d	Iodine 127	3650	AgI-U-1d	Silver	1400
Blank A-3d	Iodine 127	0.730	Blank B-2d	Silver	1400
Blank B-3d	Iodine 127	0.730	Blank C-2d	Silver	1400
Blank C-3d	Iodine 127	0.730	AgI-M-2d	Silver	1400
AgI-M-3d	Iodine 127	0.730	AgI-U-2d	Silver	1400
BiI3-M-3d	Iodine 127	730	Blank A-3d	Silver	1400
BiOI-M-3d	Iodine 127	73.0	Blank B-3d	Silver	1400
CuI-M-3d	Iodine 127	365	Blank C-3d	Silver	1400
SnI4-M-3d	Iodine 127	3650	AgI-M-3d	Silver	1400
AgI-U-3d	Iodine 127	0.730	AgI-U-3d	Silver	1400
BiI3-U-3d	Iodine 127	3650	Blank A-4d	Silver	1400
BiOI-U-3d	Iodine 127	73.0	Blank B-4d	Silver	1400
CuI-U-3d	Iodine 127	365	Blank C-4d	Silver	1400
SnI4-U-3d	Iodine 127	365	AgI-M-4d	Silver	1400
Blank A-4d	Iodine 127	0.730	AgI-U-4d	Silver	1400
Blank B-4d	Iodine 127	0.730	Blank A-7d	Silver	1400
Blank C-4d	Iodine 127	0.730	Blank B-7d	Silver	1400
AgI-M-4d	Iodine 127	0.730	Blank C-7d	Silver	1400
BiI3-M-4d	Iodine 127	365	AgI-M-7d	Silver	1400
BiOI-M-4d	Iodine 127	36.5	AgI-U-7d	Silver	1400

17 XCT Data

Table S10. Surface areas (*SA*s) as calculated geometrically and determined by XCT. The "% difference" is the increased value of *SA* measured with XCT over what was used for the ASTM C1308 tests based on geometric measurements. Note that "N/A" refers to specimens not analyzed and "–" refers to values not calculated due to a missing value from "U" or "M" samples. Also, XCT was performed on "U" coupons after leaching and "M" could not be measured because they were mounted in epoxy.

Sample set	Sample Name	Geometric *SA* (cm^2)	XCT *SA* (cm^2)	% difference
Reserve Sample (-S)	AgI-S	NA	NA	NA
	BiI_3-S	0.549	1.998	364%
	BiOI-S	0.813	1.830	225%
	CuI-S	0.868	1.751	202%
	SnI_4-S	0.477	1.757	368%
Unmounted (-U)	AgI-U	0.901	4.178	464%
	BiI_3-U	0.811	4.146	511%
	BiOI-U	0.817	2.145	263%
	CuI-U	0.975	1.827	187%
	SnI_4-U	0.762	NA	–
Mounted (-M)	AgI-M	0.316	N/A	–
	BiI_3-M	0.308	N/A	–
	BiOI-M	0.304	N/A	–
	CuI-M	0.304	N/A	–
	SnI_4-M	0.319	N/A	–

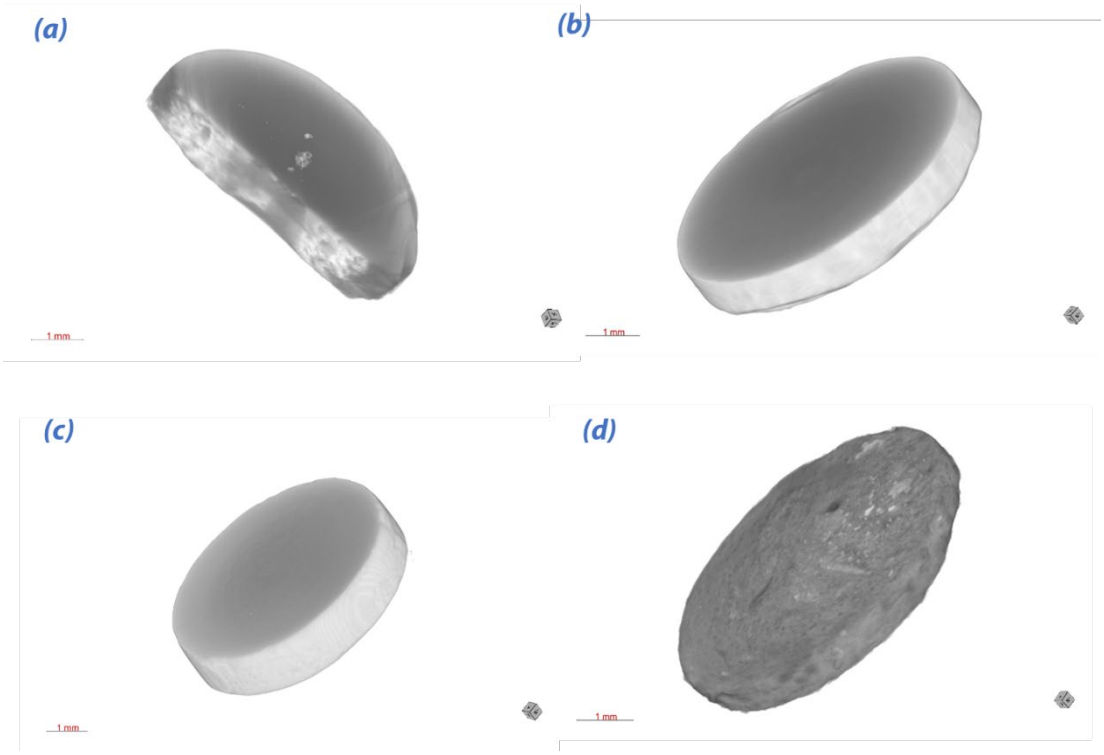

Figure S15. XCT images of the spare unleached pellets where: (a) BiI_3, (b) BiOI, (c) CuI, and (d) SnI_4.

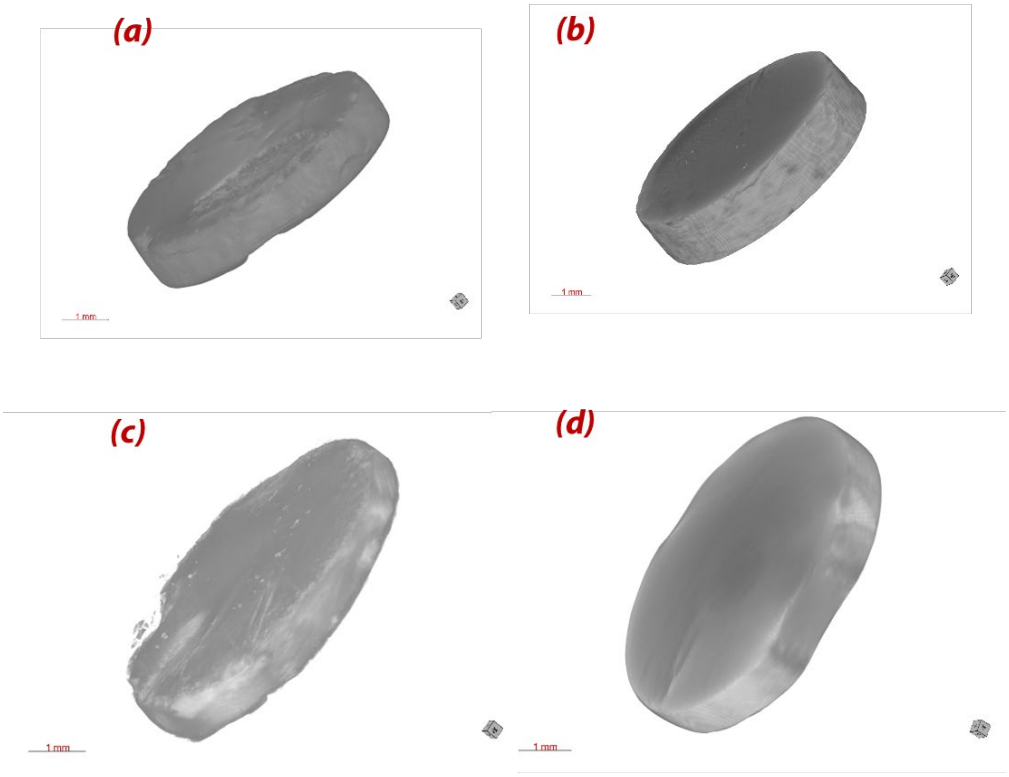

Figure S16. XCT images of the unmounted pellets post leach testing where: (a) AgI-U, (b) CuI-U, (c) BiI_3-U, and (d) BiOI-U.

18 Speculation of Other Metal Halide Compounds

Table S11. Summary of physical properties of other metal-halide compounds (halide = Cl, Br) in addition to the metal-iodide compounds discussed herein where data were available.

Metal	Comp.	T_{mp} (°C)	T_{bp} (°C)	ρ (g·cm^3)	K_{sp}	Sol (g/100g H_2O) [T]
Ag	AgCl	455	1547	5.56	1.77×10^{-10}	1.9×10^{-4}
	AgBr	430	1502	6.47	5.35×10^{-13}	1.4×10^{-5}
	AgI	558	1506	5.68	8.52×10^{-17}	3.0×10^{-6}
Bi	$BiCl_3$	234	441	4.75	–	(s)
	$BiBr_3$	219	462	5.72	–	(s)
	BiI_3	408.6	542	5.778	7.71×10^{-19}	7.8×10^{-4}
	BiOCl	575(d)	–	7.72	–	(n)
	BiOBr	560(d)	–	8.08	–	(n)
	BiOI	300(d)	–	7.92	–	(n)
Cu	CuCl	423	1490	4.14	1.72×10^{-7}	4.7×10^{-3}
	CuBr	483	1345	4.98	6.27×10^{-9}	(n)
	CuI	591	≈ 1290	5.67	1.27×10^{-12}	4.2×10^{-5}
Sn	$SnCl_4$	-34.07	114.15	2.234	–	(hyd)(hyg)
	$SnBr_4$	29.1	205	3.34	–	(s)
	SnI_4	143	364.35	4.46	–	(s)

"–" = value not found; (d) = decomposes; (hyd) = hydrolysis occurs in water; (hyg) = hygroscopic in moisture-containing atmospheres; (n) = negligible solubility; (s) = soluble in water

Table S12. Summary of SnI_x crystalline phases present in the Inorganic Crystal Structure Database (ICSD) including the space group and calculated density (ρ_c).

Phase	ICSD#	Space Group	ρ_c (g·cm^{-3})
SnI_2	2831	*C*12/*m*1	5.32
	63866	*C*12/*m*1	5.44
SnI_4	31093	*P*a-3	4.52
	36146	*P*a-3	4.55
	38140	*P*a-3	4.51
	51571	*P*a-3	4.51
	411075	*P*a-3	4.62
	415735	*P*a-3	4.52